RSC Advances

PAPER

View Article Online
View Journal | View Issue

Cite this: *RSC Adv.*, 2025, **15**, 38359

Ultrasensitive electrochemical detection of bisphenol A using copper(II) metal–organic framework ternary quantum dot (Cu-MOF/TQD) composite-modified gold electrodes

Peter A. Ajibade * and Solomon O. Oloyede

A copper(II) metal–organic framework (MOF) formulated as $[Cu_4(NITA)_4(H_2O)_2(DMF)_4]\cdot(DMF)_4$ was prepared and characterized by single-crystal X-ray crystallography. The compound crystallized as a paddled wheel binuclear complex with each copper(II) ion in a distorted square pyramidal geometry. The MOF was reacted with silver indium sulphide ($AgInS_2$) ternary quantum dots (TQDs), prepared using a hydrothermal technique, to construct a composite electrochemical sensor, formulated as {$AgInS_2$@ $[Cu_4(NITA)_4(H_2O)_2(DMF)_4]\cdot(DMF)_4$} with improved electrochemical performance. The composite was characterized by electron microscopy and spectroscopic techniques and used to fabricate modified gold electrodes as electrochemical sensors for bisphenol A determination. Cyclic voltammetry (CV) and differential pulse voltammetry (DPV) were used for the determination of bisphenol A (BPA) at the surface of each of the modified gold electrodes. The composite-modified gold electrode performed better electrochemically than the MOFs and TQDs over a concentration range of 2–20 nM (S/N = 3). The process at the surface of the composite-modified electrode was found to be diffusion-controlled, with a limit of detection of 1.33 nM and a limit of quantitation of 4.03 nM. The composite-modified gold electrode was stable, reproducible and selective and could serve as a model for the development of electrochemical sensor to determine BPA in water sample from the environment.

Received 8th August 2025
Accepted 24th September 2025

DOI: 10.1039/d5ra05819h

rsc.li/rsc-advances

1 Introduction

Indiscriminate use of organic chemicals, plastics, dyes, epoxy resins, flame retardants, polycarbonates, herbicides, pharmaceuticals and personal care products (PPCPs) has led to significant pollution of the aquatic ecosystems and public health hazards.[1–3] The preparation of polymers, plastics and rubbers involve the use of plasticizers such as bisphenol A (2,2-bis(4-hydroxyphenyl)propane or BPA). In addition, polycarbonates and epoxy resins use BPA as a chemical feedstock for their production. However, BPA is well-known as an endocrine-disrupting chemical (EDC)[4,5] with adverse effects on the body's natural hormones.[6] It has been shown that exposure to BPA can lead to serious health hazards and biological defects in unborn children and adults through increased release of prolactin,[7–9] which can trigger systemic para-inflammation.[10] This has led the governments throughout the world to set permissible limits for BPA. For instance, the maximum acceptable amount of BPA set by the European Food Safety Authority (EFSA) is 4 μg per kg bw per day.[11] Thus, it is necessary to develop an efficient method that could be used to monitor or determine trace amounts of BPA in the environment.

At present, different analytical methods are being used to quantitatively monitor BPA concentrations in the environment. These include enzyme-linked immunosorbent assays,[12] chemiluminescence immunoassays,[13] high-performance liquid chromatography,[14] molecular imprinting techniques,[15] and liquid chromatography-mass spectrometry.[16] Additionally, other analytical methods that are used include gas chromatography-mass spectrometry,[17,18] flow injection inhibitory chemiluminescence methods,[19] quartz crystal microbalance sensors,[20] and impedimetric immunosensors.[21] Furthermore, BPA has been monitored using capacitive[22] and fluorescence sensors.[23] Although high sensitivity, good selectivity, and minimal detection limits can be achieved with these techniques, their widespread use has several limitations.

In contrast, electrochemical sensors are relatively cheap, easy to prepare, offer quick reaction times, allow easy surface renewal, have high sensitivity and selectivity, and can be used for real-time detection. Different materials have been used to fabricate electrochemical sensors to increase the sensitivity and selectivity for BPA determination.[24–26] Metal–organic frameworks (MOFs) are porous materials prepared from metal ions or clusters and organic ligands/linkers.[27] MOFs possess versatile

School of Chemistry and Physics, University of KwaZulu-Natal, Private Bag X01, Scottsville, Pietermaritzburg, 3209, South Africa. E-mail: ajibadep@ukzn.ac.za

porous structures that can be adapted for various functionalities[28] and used for applications such as molecular nanomagnets,[29] catalysis,[30] energy storage,[31] drug delivery,[32] and white-light-emitting materials.[33] They are used as luminescent sensors,[34] as hybrids for boosting oxygen evolution,[35] and as sensors for phosphate ions.[36] MOF-based luminescent sensors have received considerable attention due to their ability to detect tiny molecules, cations, anions, and various analytes at different pH levels and temperatures.[37,38] Copper(II) based MOFs are good materials for luminescence due to the copper(II) d^9 electronic configuration and charge transfer transitions between the copper(II) ion and the ligand.[39] Furthermore, due to the presence of different organic linkers, the electronic absorption spectra of copper(II) based MOFs can be tuned through ligand functionalization and by modifying the coordination of the copper(II) ions and the organic linkers.[40] The fabrication method and rapid electrochemical screening were explored by Zhai *et al.* through an additive package consisting of leveler, brightener and suppressor of copper interconnects. These components are essential for the functionality, performance, power efficiency, and reliability of electronic devices, and will facilitate the future development of copper electroplating additives.[41]

Recently, bimetallic MOFs have been studied due to their unique electronic features, selectivity, and stability for different applications.[42] Previous studies[43,44] have shown that electrode materials made of bimetallic ions can exhibit much better electrochemical performance than those constructed from monometallic ions. The use of bimetallic MOFs for electrode modification to fabricate electrochemical sensors is yet to be explored for BPA detection.

Quantum dots (QDs), or colloidal nanocrystals of semiconductor materials, are inorganic fluorescent nanoparticles with sizes in the range 1 to 10 nm. These colloidal nanocrystals have unique spectroscopic characteristics with modest surface area, high extinction coefficients, photostability, high quantum yields (QY), and wide absorption and narrow emission spectra.[45,46] Composites of these semiconductors with other materials, such as dummy molecularly imprinted silica and metal–organic frameworks, have been employed in various applications, such as for the selective detection of BPA in spirit[47] and glucose in Huangshui.[48] The electronic properties of these materials can be tuned during synthesis to change their absorption band edges and emission in the visible and near-infrared regions. This feature, in addition to their potential surface interactions and conductivity with various substances, makes them valuable for the development of sensors.[49] Although many QDs have been synthesised, binary QDs (BQDs) are the most often utilised for chemical analysis. These compounds contain toxic metal ions, which are harmful to humans and pollute the environment.[50]

In this study, we present the synthesis and characterization of copper(II) metal organic frameworks (MOFs), ternary quantum dots (TQDs), and their composites (TQDs@MOFs). The compounds were used to modify bare gold electrodes to fabricate electrochemical sensors for the determination of BPA using electrochemistry techniques such as cyclic voltammetry (CV), which can be used to determine the redox potential of the analyte, study the reversibility of reactions, estimate the electron transfer kinetics, and check the stability of electrodes. Differential pulse voltammetry (DPV), in which a series of voltage pulses was superimposed on the potential, was also used to detect trace levels of analyte, measure differences in current before and after each pulse, and perform quantitative analysis. Furthermore, electrochemical impedance spectroscopy (EIS) was employed to determine charge transfer resistance, study the diffusion process, evaluate the electrode modifications, and help confirm whether the electrode surface modification improved the conductivity and kinetics.

2 Experimental

2.1 Materials and solvents

Copper(II) chloride dihydrate ($CuCl_2 \cdot 2H_2O$, 99.0% purity w/w), silver nitrate ($AgNO_3$, 99.9% purity w/w), indium chloride ($InCl_3$, 99.0% purity w/w), gelatine (99% w/w pure of protein), glutathione (GSH, 99.0% w/v purity), dimethylformamide (DMF, 99.0% w/v purity), dimethylsulfoxide (DMSO, 99.9% w/v purity), thioglycolic acid (TGA, 99.9 w/v purity), distilled water, deionized water, ultra-pure water, methanol (MeOH, 99.0% w/v purity), ethanol (EtOH, 99.0% w/v purity), bisphenol A (BPA, 99.8% w/w purity), potassium ferricyanide ($K_3[Fe(CN)_6]$, 99.0% w/w purity), potassium chloride (KCl, 99.8% w/w purity), sodium hydroxide (NaOH), and 5-nitroisophthalic acid (NITA, 99.0% w/w purity) were all purchased from Sigma-Aldrich, St Louis, Missouri, USA and used without further purification. All other chemicals and reagents were of analytical grade.

2.2 Physical characterization

Scanning electron microscopy (SEM) was conducted using ZEISS FEGSEM ultra plus (Oberkochen, Germany) with a rating voltage of 15–20 kV at various magnifications (as shown in the SEM micrographs) to obtain the surface morphology of the compounds. A JEOL JEM-2100 electron microscope (Akishima, Tokyo, Japan) was used to capture transmission electron microscopy (TEM) images, which show the shapes of the compounds. On a Bruker Alpha FTIR spectrometer (Manufacturer: Bruker, 40 Manning Road, Billerica, MA 01821, Massachusetts, USA) fitted with an attenuated total reflection (ATR) platinum diamond, Fourier transform infrared (FTIR) spectra were collected for the identification of various functional groups in the compounds over a specific spectral range of 4000–500 cm^{-1}, resolution of 1 cm^{-1}, signal-to-noise ratio of $\geq$50 000 : 1, and using a suitable detector (DLATGS).

Dimethylsulfoxide (DMSO) and methanol (MeOH) at room temperature were employed to dissolve the compounds, and the ultraviolet-visible (UV-Vis) spectra were obtained on a PerkinElmer Lambda 25 UV-Vis spectrophotometer (38 McPherson St. Markham, ON, Canada, L3R 3V6). A Stuart SMP3 melting point device (625 East Bunker Court, Vernon Hills, IL 60061–1844) was used to record melting points. An electrochemical workstation Autolab PGSTAT 302N (Metrohm Autolab B.V. at Woudwetering 3–5, Utrecht, 3543 AV, Netherlands), with an

electrochemical impedance spectroscopy module (EISM), was used for all electrochemical investigations, including differential pulse voltammetry (DPV), cyclic voltammetry (CV), and electrochemical impedance spectroscopy (EIS).

For the electrochemical experiments at ambient temperature, a standard three-electrode setup was used, including a platinum (Pt) counter electrode, which completed the circuit by allowing the flow of current, silver/silver chloride potassium chloride (Ag/AgCl|KCl (sat.)) wire, as a pseudo reference electrode, which provides a stable, known potential against which the working electrode's potential is controlled and measured, and a gold working electrode, where the reaction of interest occurs (*i.e.* redox reaction of the analyte). These electrodes were obtained from Metrohm Autolab B.V., Woudwetering 3–5, Utrecht, 3543 AV, Netherlands.

2.3 Synthesis of $[Cu_4(NITA)_4(H_2O)_2(DMF)_4]\cdot(DMF)_4$ (1)

The synthetic method of Mondal *et al.*[51] was adopted with modifications as shown in Scheme 1. Copper(II) chloride dihydrate $(CuCl_2)\cdot 2H_2O$ (4 mmol, 0.680 g) was dissolved in 10 mL of *N*,*N*-dimethylformamide (DMF) and stirred at room temperature for 20 min, and 5-nitroisophthalic acid (4 mmol, 0.844 g) dissolved in 30 mL of DMF/water (2 : 1) was added. A greenish-blue clear solution was obtained, which was stirred at room temperature for 30 min, then refluxed at 70 °C for 4 h. The clear blue filtrate was kept at room temperature for slow evaporation,

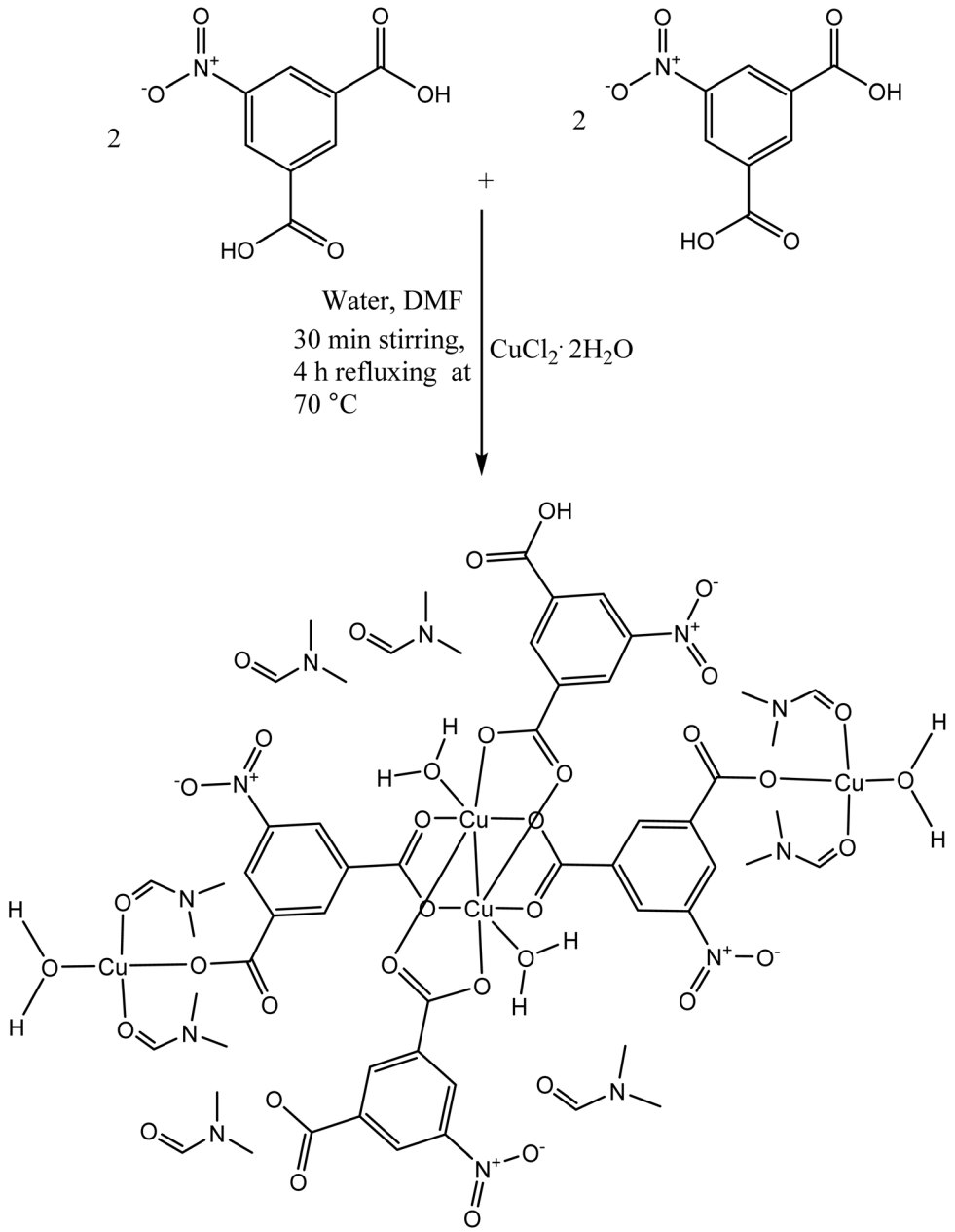

Scheme 1 Synthesis of the $[Cu_4(NITA)_4(H_2O)_2(DMF)_4]\cdot(DMF)_4$ MOF.

and, after five weeks, blue crystals were harvested from the solution. The crystals obtained were washed with DMF/water (1 : 1), dried at room temperature, and kept in a desiccator for further characterization. Yield: 87% (1.325 g), M. pt. 478 °C. Anal. found (calculated): $C_{53}H_{69}Cu_4N_{11}O_{35}$ (%): C: 38.12 (38.01); H: 4.12 (4.16); N: 9.20 (9.27); O: 33.47 (33.21).

2.4 Single-crystal X-ray crystallography of compound 1

Single crystals suitable for X-ray crystallographic analysis of compound **1** were obtained through slow evaporation of a DMF and water solution of the compound. Single-crystal X-ray diffraction data were collected on a Bruker D8 Venture diffractometer using graphite-monochromated Mo-Kα radiation (χ = 0.71073 Å). Data collection was carried out at 100(2) K. The temperature was controlled with an Oxford Cryostream cooling system (Oxford Cryostat). Cell refinement and data reduction were performed using the program SAINT.[52] The data were scaled, and absorption correction was performed using SADABS.[53] The structure was solved by direct methods using SHELXS-97 (ref. 53) and refined by full-matrix least-squares methods based on F^2 using SHELXL-2014 (ref. 53) and using the graphics interface program X-Seed.[54,55] The programs X-Seed and POV-Ray[56] were used to prepare molecular graphics images.

All non-hydrogen atoms were refined anisotropically. All hydrogen atoms, except the hydrogens on O31 and O32, were placed in idealised positions and refined in riding models with U_{iso} assigned 1.2 or 1.5 times the U_{eq} of their parent atoms, and the C–H bond distances were constrained to 0.95 Å or 0.98 Å. The hydrogen atoms on O31 and O32 could not be located in the difference density maps and were excluded from the final model. One of the DMF solvent molecules was disordered over two positions, each with half-site occupancies. The structure was refined to an R factor of 0.0573.

2.5 Synthesis of $AgInS_2$ ternary quantum dots (TQDs) (2)

The synthetic method of Castro *et al.*[57] was used with some modifications. TGA (1 mL) was added to water (10 mL), and the mixture was stirred for 10 min. Then, $Ag(NO_3)$ (0.175 g, 1 mmol) in 10 mL of distilled water was added to the solution of TGA and stirred for 20 min at room temperature. This was followed by the addition of $InCl_3$ (0.293 g, 1 mmol) in 5 mL of distilled water, and the three components were refluxed for 45 min at 70 °C. Sodium sulphide Na_2S (1 mmol, 0.78 g) in 10 mL distilled

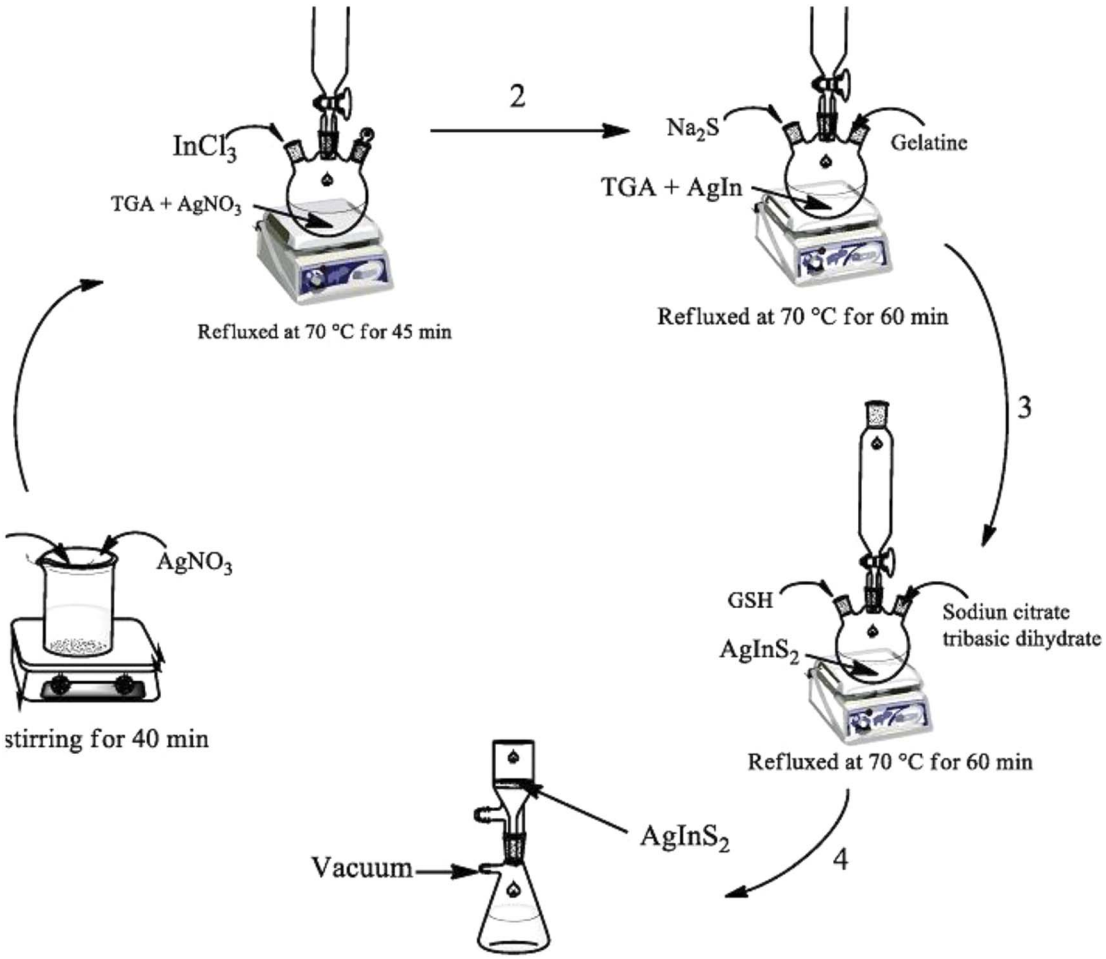

Scheme 2 : Proposed synthesis of $AgInS_2$ (TQDs).

water was then added slowly to the hot solution of AgIn, followed by the addition of gelatine (1 mmol, 0.180 g), then the whole mixture was refluxed for 60 min at 70 °C. Glutathione (0.309 g, 1 mmol) was added to the refluxing mixture, followed by sodium citrate tribasic dihydrate (0.294 g, 1 mmol) to aid the dispersion of the as-prepared ternary quantum dots. Subsequently, 5 mL methanol was added to precipitate the product. This precipitate was centrifuged at 5000 rpm for 7 min, filtered and dried in an oven at 35 °C for 10 min (Scheme 2).

2.6 Synthesis of composite (TQDs@MOFs) $\{AgInS_2@[Cu_4(NITA)_4(H_2O)_2(DMF)_4]\cdot(DMF)_4\}$

2.6.1 Compound 3. The synthesis of the composite (TQDs@MOFs) was achieved using the one-pot synthetic method, also known as "the bottle around the ship" by Fu *et al.*,[58] with some modifications. In this method, copper(II) chloride dihydrate (4 mmol, 0.680 g) was dissolved in 15 mL DMF and stirred at room temperature for 10 min. The homogeneous solution of the crushed pre-synthesized $AgInS_2$ (0.65 g) in 10 mL water, was then added and stirred for 20 min. 5-Nitroisophthalic (4 mmol, 0.844 g) in 10 mL DMF was then added to the above mixture, which was then stirred at room temperature for 12 h. The composite $\{AgInS_2@[Cu_4(NITA)_4(H_2O)_2(DMF)_4]\cdot(DMF)_4\}$ suspension was precipitated by the addition of 1 mL ethanol. The composite was then centrifuged at 5000 rpm for 7 min, collected *via* decantation, washed with DMF/H_2O (1 : 1), and incubated in an oven at 30 °C for 45 min. Percentage yield: 70% (1.52 g).

2.7 General electrode modification

The drop-dried method of modifying electrode surfaces is frequently used for binding nanomaterials on the surface of bare gold electrodes. Piranha solution was used to clean the electrodes, which were then washed with water and acetone, polished with 0.5 μM alumina paste, and then washed once more with ultra-pure water. After cleaning, the exposed electrodes were dried under nitrogen gas. A homogeneous dispersed solution was obtained after 10 min of ultrasonic agitation of 5 mg of compound **1**, which was dissolved in water. With the aid of a micropipette, a few drops of the suspension of compound **1** were applied to the surface of the cleaned gold electrode. The optimum conditions were attained by drying the dispersed dropped solution of compound **1** onto the surface of the bare electrode in an oven at 35 °C for 30 min. To remove unattached materials, the modified gold electrode was washed with an appropriate solvent after drop drying. Finally, the modified electrode was dried using dry nitrogen gas to eliminate residual solvent.

3 Results and discussion

3.1 Molecular structure of the copper(II) metal organic frameworks

Single-crystal X-ray crystallography of the copper(II) MOF revealed the binuclear copper(II) complex, $[Cu_4(NITA)_4(H_2O)_2(DMF)_4]\cdot(DMF)_4$, with four *N*,*N*-dimethylformamide molecules acting as a solvent of crystallization within the crystal lattice. The molecular structure of compound **1** is presented in Fig. 1

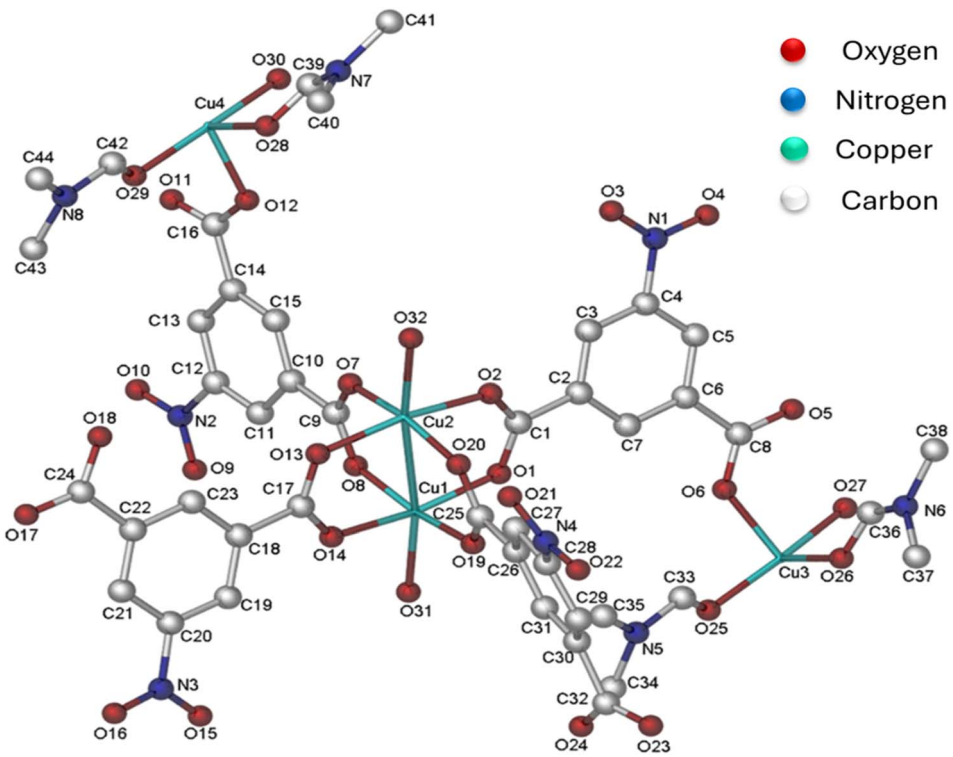

Fig. 1 ORTEP diagram of $[Cu_4(NITA)_4(H_2O)_2(DMF)_4]\cdot(DMF)_4$ (**1**), showing the spatial arrangement of molecules and atoms with numbers.

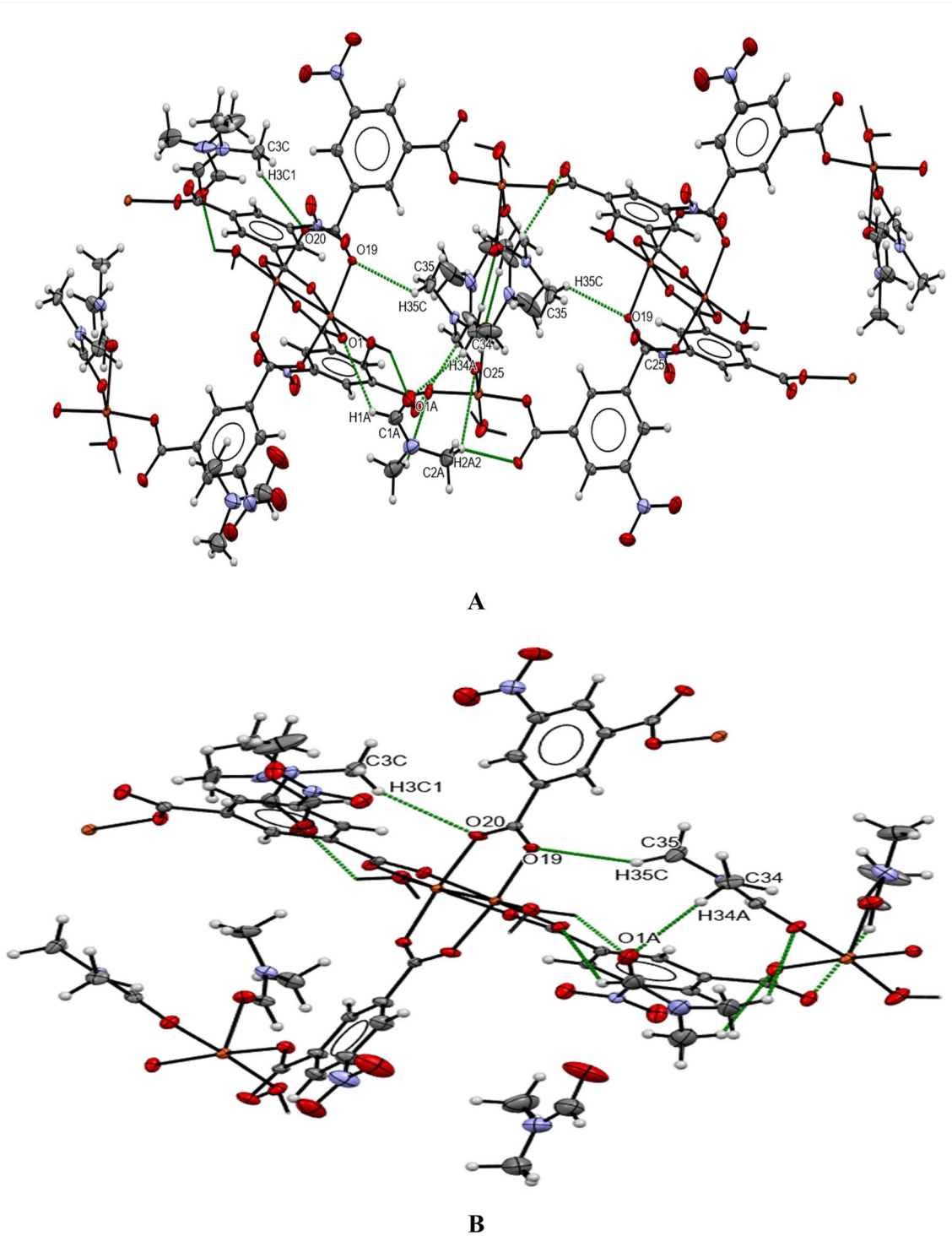

Fig. 2 ORTEP diagram showing hydrogen bonding of $[Cu_4(NITA)_4(H_2O)_2(DMF)_4]\cdot(DMF)_4$ through the *a*-axis (A) and *b*-axis (B).

with the oxygen atoms shown in red, nitrogen atoms in blue, carbon atoms in grey, and copper(II) in green. The packing diagram of compound **1** contained four molecules in the unit cell, and the ORTEP diagram of **1** shows hydrogen bonding through the "*a*-axis" and "*b*-axis" (Fig. 2 and S1). The crystal data and structure refinement of **1**, together with selected bond lengths and bond angles, are presented in Tables T1 and T2. Compound **1** crystallises in a $P2_1/c$ space group in a monoclinic crystal system, which forms a discrete binuclear molecule as shown in Fig. 1. Copper(II) ions in compound **1** are coordinated to four molecules of 5-nitroisophthalic acid (NITA), acting as bidentate ligands to form a paddlewheel copper(II) carboxylato structure. Each of the copper(II) ions is coordinated at the equatorial plane to four carboxylato planar oxygen donor atoms

from each of the four bidentate NITA ligands, and one oxygen atom from a water molecule coordinates at the axial position to each of the copper(II) ions. The basal planes at each equivalent copper(II) ion consist of four planar carboxylato oxygen atoms bonded to the copper(II) ion. The molecular structure of **1** revealed a five-coordinate (pentagonal) geometry around each equivalent copper(II) ion with a Cu···Cu intermetallic separation bond. The four bidentate NITA ligands are approximately perpendicular to each other through their coordination bond with each binuclear copper(II) ion.

The bond angles Cu1–Cu2–O32 (172.71°) and Cu2–Cu1–O31 (171.63°) deviate from linearity along the Cu1–Cu2 and O31–O32 axes. Two of the four NITA ligands are almost coplanar, as the coplanarity of the two NITA ligands may be elucidated by the plane formed by the two equivalent copper(II) ions and the four carboxylato oxygens, with these angles being closer to 180°. The interplanar distance (intermetallic bond) between the two basal planes is 2.6358(7) Å [Cu1–Cu2 = 2.6358(7) Å], which is similar to the intermetallic bond distance of 2.64 Å in other copper(II) binuclear complexes.[59,60] The Cu–O bond lengths (1.959–1.982 Å) at the equatorial axes around the copper(II) ions are similar to those obtained in other binuclear copper(II) complexes,[61–63] and the bond lengths of Cu–O at the apical axes (2.163(3) Å for Cu1–O32 and 2.158(3) Å for Cu2–O31) are also similar to those of other reported binuclear copper(II) complexes (2.100–2.300 Å).[64–66] The geometry around the two equivalent copper(II) ions are a slightly distorted square pyramidal based on the Addison parameter (Tau (τ) with this equation $\tau = (\beta - \alpha)/60$, where '$\beta$' and '$\alpha$' are the first and second largest angles, respectively) around each copper(II) ion of the binuclear complex. Thus, the calculated value of τ for Cu1 is 0.006 and that of Cu2 is 0.003, which are closer to zero (0) than unity (1). This is further confirmed by the angles around the copper(II) ions, which are almost 90°. The polyhedral geometry of **1** (Fig. S2) further confirmed the distorted square pyramidal geometry around each copper(II) ion. The packing diagram revealed that the four asymmetric units are linked through classical intermolecular and intramolecular hydrogen bonding, which contributes to the stability of the compound. The four DMF solvents of crystallization are connected *via* classical intermolecular non-covalent interactions that form an infinite three-dimensional chain. Fig. S2 further supports the stability of **1** through a view of its extended network along the *a*-axis.

Through positions "*a*" and "*c*", the crystal compound was purposely packed to visualise the presence of solvent or tiny molecules inside the crystal lattice. It is possible to trap small molecules in the crystal pore (Fig. 3). The void space through the contact surface (Fig. 3A) of the crystal was explored at a radius of 0.3 Å and an approximate grid spacing of 2 Å. Its volume, 2114.45 Å^3, represents 31% of the unit cell volume. In addition, the void space through solvent-accessible surface (Fig. 3B), probed at 0.2 Å with 1 Å grid spacing, had a volume of 922.86 Å^3, which is 13.5% of the unit cell volume.

3.2 FTIR spectroscopic studies of the compounds

The bands in the range 3300–3200 cm^{-1} in the free ligands and the copper(II) complex spectra are attributed to the ν(O–H) stretching frequency of the carboxylic group[67] (Fig. S4). The band at 1705 cm^{-1}, attributed to ν(C=O) in the free ligand, shifted to 1643 cm^{-1} in the spectrum of the complex.[68] The bands in the range 1351–1248 cm^{-1} in the spectra of the complex and the free ligand are assigned to ν(C–O) stretching vibrations. The band observed in the range 700–600 cm^{-1} is

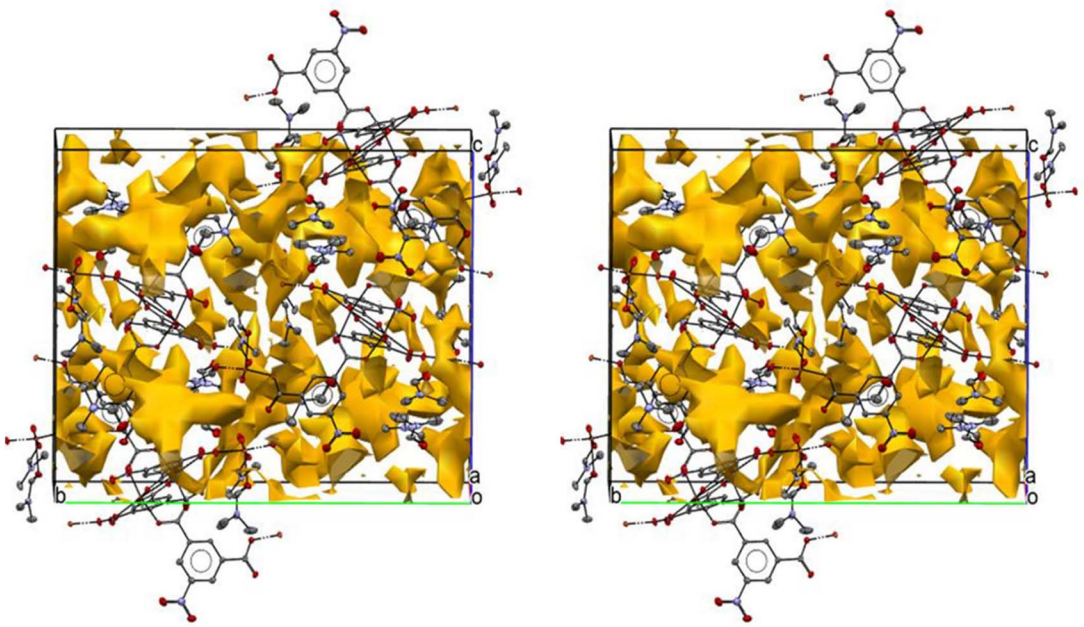

(**a**) (**b**)

Fig. 3 Void space through the contact surface (a) and solvent accessible surface (b) showing the porosity of $[Cu_4(NITA)_4(H_2O)_2(DMF)_4]\cdot(DMF)_4$ (**1**).

assigned to ν(C=C) bending vibrations.[69] The ν(C–N) band at 1095 cm^{-1} in the free ligand shifted to 1075 cm^{-1} in the complex. The $\nu(NO_2)$ stretching frequency appearing at 1456 cm^{-1} in the spectrum of the free ligand shifted to 1431 cm^{-1} in the spectrum of the complex.[70] The bands at 597 cm^{-1} and 469 cm^{-1} in the spectrum of the complex are assigned to ν(Cu–O) and ν(Cu–Cu) stretching vibrations.

The spectrum of the GSH shows ν(N–H), ν(O–H) (carboxylic), and ν(C=O) stretching vibrational bands at 3300 cm^{-1}, 3100 cm^{-1}, 1720 cm^{-1}, respectively, with the ν(C–N) bending vibration at 1360 cm^{-1}. A weak ν(S–H) band of the GSH is observed at 2550 cm^{-1}. The spectrum of the gelatine also shows ν(C–N), ν(O–H), ν(C=O), ν(N–H), ν(C–H), and ν(C–C) stretching vibrational bands at 2160 cm^{-1}, 3550 cm^{-1}, 1730 cm^{-1}, 3400 cm^{-1}, 2860 cm^{-1}, and 1550 cm^{-1}, respectively. The ν(C–H) bending vibration appeared at 1425 cm^{-1}. The stretching vibration bands for both compounds are also present in the spectrum of the TQD, confirming its formation. The band observed at 3300 cm^{-1} is assigned to ν(N–H) of GSH, the ν(O–H) of the gelatine appeared at 3200 cm^{-1}, and the ν(C–N) appeared in the range of 2160–2300 cm^{-1}, while the ν(C=O) of gelatine appeared at 1720 cm^{-1}. The vibration band observed at 553 cm^{-1} is attributed to the ν(Ag–In). These results confirmed the presence of hydroxyl, carboxyl, and amine functional groups from gelatine, and GSH acts as a passivating agent on the surface of the QDs, rendering it soluble in water[71–75] (Fig. S5).

The FTIR spectrum of compound **3** shows major stretching vibrations at 597 cm^{-1}, 553 cm^{-1}, and 469 cm^{-1}, that are assigned to ν(Cu–O), ν(Ag–In), and ν(Cu–Cu) in the spectra of the copper(II) metal–organic framework and ternary quantum dots, respectively. The ν(O–H), ν(C–H), and ν(N–H) from the TQDs and MOFs in the composites were observed at 3252 cm^{-1}, 2899 cm^{-1}, and 3475 cm^{-1}. This confirms the synthesis of the composite. Other major vibrational bands from the MOFs such as ν(C–C), ν(C–O), ν(C–N), and ν(C=O) were observed at 1521 cm^{-1}, 1345 cm^{-1}, 1075 cm^{-1}, and 1634–1700 cm^{-1}, respectively, in the composite[76] (Fig. S6).

3.3 Electronic spectroscopic studies of the compounds

The electronic spectrum of the composite shows that the absorption bands found in the MOFs and TQDs have slightly shifted. The electronic spectrum of the MOF (**1**) (Fig. S7A) shows absorption bands at 240 nm and 285 nm, attributed to the ligand-to-metal charge transfer transitions. Other bands observed at 562 nm and 637 nm are assigned to the d–d transition of copper(II).[77,78] The spectrum of the TQD (**2**) (Fig. S7B) shows three major absorption bands. The absorption at 204 nm is assigned to the $\pi \rightarrow \pi^*$ electronic transition of gelatine. The other two absorptions at 244 nm and 283 nm could be attributed to the $\pi \rightarrow \pi^*$ and $n \rightarrow \sigma^*$ transitions of glutathione.[79] The spectrum of composite (**3**) (Fig. S7C) shows a hypochromic shift at 510 nm and a bathochromic shift at 657 nm, similar to the spectrum of MOFs, which were attributed to the excitation of an electron in the d orbital of Cu^{2+} through d–d and MLCT transitions. With regard to the TQDs, the spectrum of the composite shows a bathochromic shift at 207 nm and 252 nm, which were attributed to the $\pi \rightarrow \pi^*$ transition of gelatine and to the $n \rightarrow \pi^*$ transition in the glutathione.

The calculated energy band gaps (Fig. S8) of the compounds are 3.753 eV for the copper(II) MOFs, 4.155 eV for the composite, and 5.489 eV for the TQDs. The energy band gap of the composite is higher than that of the MOFs but lower than that of the TQDs, which suggests that there are good interactions between the MOFs and TQDs to form the composite with a blend of their electronic properties.

3.4 Powder X-ray diffraction patterns of the compounds

Powder X-ray diffraction patterns of the MOFs, TQDs, and their composite are shown in Fig. S9. The 2θ peaks at 10°, 20°, and 25° in the diffraction patterns of the TQDs are attributed to the (100), (111), and (112) lattice planes of an orthorhombic silver selenide structure, which are also present in the diffraction patterns of the composite but with very low intensity, indicating the amorphous nature of the TQDs.[80] The 2θ peaks at 30°, 40°, 45°, and 50°, in the diffraction patterns of the MOFs are ascribed to the (400), (420), (422), and (440) lattice planes, with the ordered cubic lattice structure of copper(II) 1,3,5-benzenetricarboxylate also present in the diffraction patterns of the composite.[81] The presence of peaks at 10°, 25°, 30°, and 40° in the diffraction patterns of the composite confirms the mixed crystalline phases of the composite (Fig. S9).

3.5 Morphological studies of the compounds

SEM micrographs of the compounds are presented in Fig. S10(A1–C1). Compound **1** exhibits a layered sheet-like surface morphology. Their sharp edges and flat surfaces are stalked angularly, which is typical of crystalline structures that are randomly stacked and overlap to form hierarchical patterns. The uniformly smooth and flat surfaces of the particles suggest well-formed crystalline facets with no crisp corners and edges, indicating no deformation and retention of the original crystalline shape during the synthesis. The existence of voids between the particles implies a porous network.[82]

The SEM micrograph of compound **2** consists of long, rod or needle-like surface structures arranged in a densely packed, overlapping pattern. The uniformity of the rods may suggest a self-assembly, hydrothermal growth process. The sharp edges indicate good crystallinity and controlled morphology. The material's mechanical stability was improved by the random nanorods that form an interconnected network with some stacking. The presence of overlapping and bundled rods gives the sample a rough overall texture.[83]

The micrograph of compound **3** revealed rod-like structures and plate-like features. The surface morphology is densely packed, as observed for compound **2**, while the plate-like structures appeared scattered throughout, as in compound **1**, with some oriented at different angles, which suggests the presence of crystalline or layered structures. The observed differences in morphologies could indicate a mixed-phase material or different crystallization conditions during the synthesis, and the sharp edges of the plates point to high crystallinity, which indicates a controlled growth process.[84]

TEM micrographs of compounds **1**, **2**, and **3** are presented in Fig. S10(A2–C2), respectively. Compound **1** exhibits a plate-like particle structure. These platelets are arranged hierarchically by random overlapping and stacking. The particles' uniformly smooth, flat surfaces point to well-formed crystalline facets with crisp corners and edges, which suggest that they were not deformed, and could mean that their original crystalline shape was maintained during the synthesis or growth process. The dark areas indicate that the material has an aggregated structure, with individual plate-like particles loosely packed together. A porous network is indicated by the apparent presence of inter-particle spaces.

The TEM micrograph of compound **2** revealed agglomerates of closely packed, rod-like structures and some spherical particles. The particles' undefined edges raise the possibility that they are amorphous. Materials made *via* solvothermal methods exhibit this kind of aggregation, where the particles group together to reduce surface energy. Based on the observable fine structures, the aggregate's individual primary particles seem to be between 10 and 50 nm in size.[84] The TEM micrograph of compound **3** revealed a plate-like material characterised by semi-transparent and flat dominating structures, suggesting the presence of a transition metal. Differences in contrast within the same structure reveal a composite compound with uneven edges and varied thickness. The presence of nanoparticles deposited on the sheets is indicated by the dark, rounded features throughout the surface of the sheet-like formations. A composite material with nanoparticles supported on the substrate is confirmed by such characteristics.[85] The nanoparticles that are visible on the sheets are widely distributed and range in sizes from 5 to 20 nm. Their uniform distribution suggests a controlled synthesis process, which could improve properties such as sensing performance.

3.6 Activation and modification of the bare gold electrode

The bare gold electrode surface was polished with alumina slurry (0.3 μm and then 0.05 μm) on a microcloth and rinsed thoroughly with deionized water. It was later used to perform cyclic voltammetry (CV) in 0.5 M H_2SO_4 (scan between −1.5 V to 1.5 V *vs.* Ag/AgCl|KCl (sat.)) until a stable voltammogram was obtained. It was thereafter rinsed with deionized water and dried under nitrogen before the surface was activated through immersion in piranha solution (3 : 1 H_2SO_4/H_2O_2) for 10–15 minutes. The bare electrode was finally rinsed thoroughly with deionized water before further modification. The drop-dry (drop-casting) method of modification was used to improve the surface of the bare gold electrode (AuE).[86] This technique modifies the surface of the bare electrode by first depositing a drop of the liquid containing a suspension of the particles of interest. To create a homogeneous suspension, 5 mg of each component was dissolved in 10 mL of ultra-pure water and then sonicated. The suspension was cast over the bare electrode's surface and then transferred into a UV lamp chamber to dry under a nitrogen flow. The UV lamp helped to activate the materials on the surface of the electrode and facilitated the removal of residual solvent from the active surface. The nitrogen prevents the oxidation of the materials at the surface of the modified electrodes, prevents contamination from moisture, and speeds up solvent evaporation.

3.7 Electrochemical impedance spectroscopy (EIS)

Electrochemical impedance spectroscopy (EIS) and cyclic voltammetry (CV) were used to determine the electrochemical response of the bare and modified electrodes with compounds **1**, **2**, and **3**. Under an applied frequency range of 100 kHz to 0.1 Hz, EIS measurements were conducted in a supporting electrolyte of 5 mM $K_3[Fe(CN)_6]$ in 0.1 M KCl. Nyquist plots, shown in Fig. 4(A–D) (A: bare electrode; B: electrode modified with **1**; C: electrode modified with **2**; D: electrode modified with **3**), were used to determine the impedance across the modified electrodes. The electrolyte resistance (R_s), charge transfer resistance (R_{ct}), which is calculated as the diameter of the semi-circle that appears at a higher frequency, Warburg impedance (Z_w), which is the semi-circle that appears at a lower frequency, and the constant phase element (CPE) make up the Randle's equivalent circuit for the bare and modified electrodes (Fig. 4(E)). The results indicate the surface of the bare and modified electrodes showed a range of responses, which varies from a straight-line response for the bare and electrodes modified with compound **3** (indicating a diffusion system: low impedance) to a curve shaped and an arch or a quarter circle shaped line at the lower energy frequency (indicating the limit to the charge transfer) for the electrodes modified with compounds **1** and **2**, respectively. A summary of the R_{ct}, Z_w, R_s, and CPE values is given in Table 1, which represents the electrochemical impedance spectroscopy data obtained for 5 mM $K_3[Fe(CN)_6]$ in 0.1 KCl at the bare electrodes and electrodes modified with compounds **1**, **2**, and **3**. The R_{ct} values at the surface of the bare electrode and electrodes modified with compounds **1**, **2**, and **3** are 52.7 Ω, 68.7 kΩ, 45.8 Ω, 3.88 Ω, respectively. The findings supported the previously proposed hypothesis, which indicates that the composite-modified electrode with the lowest charge transfer resistance value of 3.88 Ω could be regarded as the most reactive electrode that would transfer electrons from the analyte to its surface more quickly than the other electrodes, which enhances the electrode's sensing and detection response.[87] The exponential value of CPE '*n*' in relation to the depression angle is less than unity ($n < 1$). This accounts for the non-ideal capacitive behaviour of the electrodes due to surface roughness and diffusion effects.[88] Fig. 5 shows that the electrodes' phase angles in the Bode plots are less than 90°, which is the angle for a perfect capacitor, which further confirms their non-capacitive nature.[89]

3.8 Electrochemical responses of 5 mM potassium ferricyanide $K_3[Fe(CN)_6]$ in 0.1 M potassium chloride (KCl) at the surface of the bare and modified electrodes at pH 7

Cyclic sweep ranges of −0.2 V to 0.5 V, −0.15 V to 0.30 V, −0.35 V to 0.4 V, and 0.0 V to 0.9 V at the surface of the bare electrode and electrodes modified with compounds **1**, **2**, and **3**, respectively, are presented in Fig. 6(A1–D1). Plots of the oxidative peak current responses (I_{pa}) *vs.* the square roots of the scan rate ($\nu^{1/2}$) with scan rate increase from 100 to 300 mV s^{-1}, in addition to

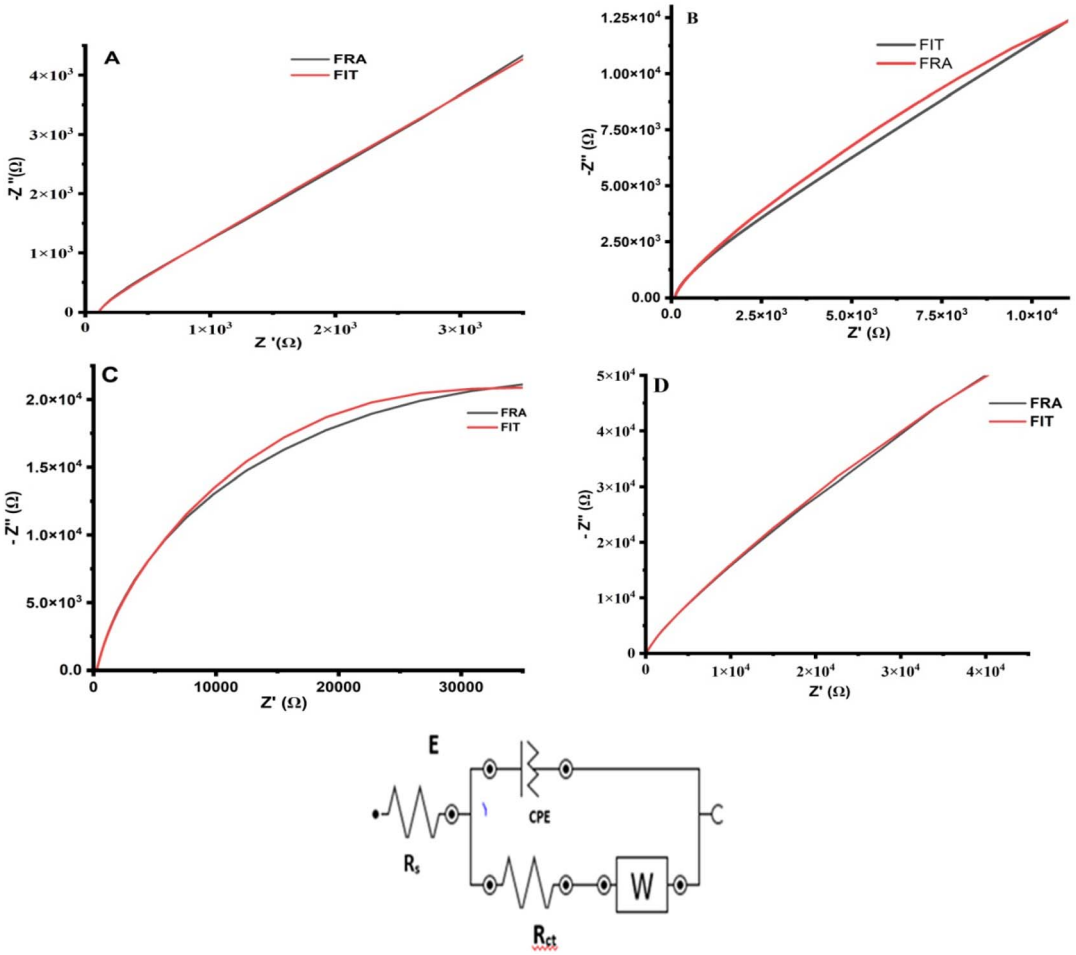

Fig. 4 Nyquist plots of the compounds (A–D), illustrating the response of electron transfer at the surface of the bare electrode and electrodes modified with **1**, **2**, and **3**, respectively. Randle's equivalent circuit (E) employed to determine the impedance at the surface of the bare electrode and electrodes modified with **1**, **2**, and **3**.

the regression plots, are presented in Fig. 6(A2–D2) for the bare electrode and electrodes modified with compounds **1**, **2**, and **3**, respectively. From the cyclic voltammograms, the surface of the gold electrode modified with compound **2** showed an irreversible electrochemical response, with only an oxidation peak current (I_{pa}) and no reduction, which indicates that the reaction at its surface may be an irreversible adsorption-controlled process.[90] Redox reactions are clearly visible at the surface of the bare electrode and electrodes modified with compounds **1** and **3**. The forward scan showed an oxidation peak current (I_{pa}) response, and the reverse scan showed no reduction peak current (I_{pc}). With the exception of the electrode modified with compound **2**, the responses of potassium ferricyanide at the surface of these electrodes showed that an increase in scan rate results in an increase in the oxidation (I_{pa}) and reduction (I_{pc}) peak currents. This rise in oxidation peak current with increase in scan rates, with the values of the regression coefficient (R^2), indicates that the oxidation process at these electrodes' surface is a diffusion-controlled electrochemical reaction on the forward scan.[91]

Table 1 Electrochemical impedance spectroscopy data obtained for 5 mM $K_3[Fe(CN)_6]$ in 0.1 KCl at the bare electrode and electrodes modified with compounds **1**, **2**, and **3**[a]

Au electrodes	R_s (Ω)	R_{ct}	Z_w (μMho)	CPE (μMho)	n
Bare	106	52.7 Ω	125	16.6	0.855
Electrode modified with compound **1**	101	68.7 Ω	14.4	7.19	0.864
Electrode modified with compound **2**	251	45.8 kΩ	55.4	4.65	0.823
Electrode modified with compound **3**	103	3.88 Ω	23.2	7.76	0.821

[a] "n": the exponential value of CPE related to the depression angles.

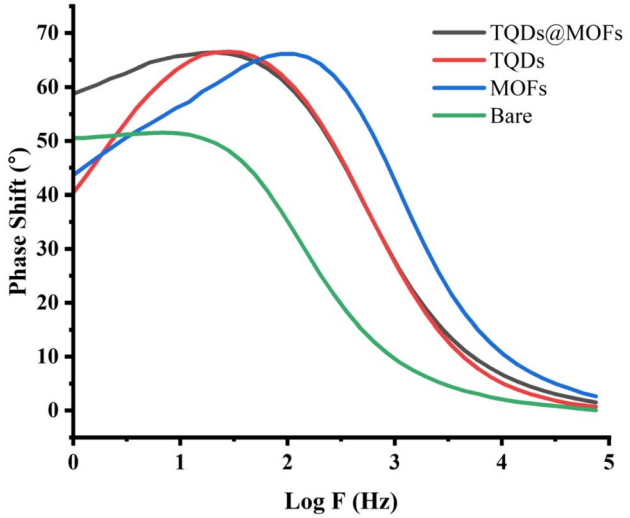

Fig. 5 Bode phase plots, illustrating the phase angles obtained at the surface of the bare electrode and electrodes modified with MOFs (**1**), TQDs (**2**), and TQDs@MOFs (**3**).

Nicholson's theory states that a decrease or low magnitude of the separation peak potential ΔE_p ($E_{pa} - E_{pc}$) (*i.e.*, $\Delta E_p < 300$ mV, where E_{pa} is the oxidation peak potential and E_{pc} is the reduction peak potential) causes the heterogeneous rate constant (k^o) to increase, an indication of electron transfer between the modified electrode's surface and the analyte to be sensed/determined. The values of separation peak potentials and the oxidation peak currents at the surface of each modified gold electrode are given in Table 2. It could be observed that the highest oxidation peak current (I_{pa}) and the smallest separation peak potential (ΔE_p) are obtained at the surface of the composite-modified gold electrode, which indicates that the best electrochemical response is observed at the surface of the modified electrode.[92]

3.9 Electrochemical determination of bisphenol A (BPA) at the surface of the modified electrodes

The three electrodes used for this study were a gold (Au) working electrode, a platinum with Ag/AgCl|KCl (sat.) wire as the reference electrode, and a platinum as the counter electrode on an Autolab PGSTAT 320 N electrochemical workstation. The electrodes were cleaned with redistilled deionized water and anhydrous alcohol, then dried under nitrogen before use. All solutions were deoxygenated by bubbling them with nitrogen for 10 minutes. Before each measurement, the working electrode was treated with a PBS solution (pH 7). Fig. 7(A1–C1) shows the response of the modified electrodes with compounds **1**, **2** and **3** against 2 nM solution of BPA. The plots of the oxidation peak current responses (I_{pa}) *vs.* the square root of the scan rates ($\nu^{1/2}$) at the surface of each modified gold electrode with compounds **1**, **2**, and **3** are presented in Fig. 7(A2–C2). Cyclic sweeps ranged from −0.6 V to 0.2 V, 0.3 V to 0.9 V, and −0.1 V to 1.4 V at the surface of the modified electrodes. A complete electrochemical redox response (oxidation and reduction) occurred at the surface of the modified electrodes, which indicates a reversible reaction at the surface of these electrodes, whereas only an oxidation response occurred at the surface of the electrode modified with compound **2**, indicating an irreversible response as predicted from the study of the potassium ferricyanide. From the voltammograms obtained at the surface of these modified electrodes, an increase in the scan rate led to an increase in the oxidation peak current response and an increase in the reduction peak current at the surface of the modified electrodes. The relationship between the oxidation peak current response and the scan rate suggests that the electrochemical determination of BPA at the surface of these modified electrodes is a diffusion-controlled process. The values of the regression coefficient are 0.5 to 1.0 ($0.5 < R^2 < 1$) from the plots of the oxidation peak current response and the square root of the scan rate, further confirming that the process is diffusion-controlled.[93] The values of the oxidation peak current responses at the surface of the modified electrodes and their coefficients of regression are presented in Table 3. The results show that the composite-modified electrode has the highest oxidation peak current response, with a value of 1.27×10^{-3} μA, in contrast to 7.26×10^{-5} for MOFs and 1.137×10^{-5} for TQDs, which is in agreement with the results obtained with potassium ferrocyanide. This indicates fast movement and adequate transfer of electrons between the bisphenol A (preference analyte) and the composite at the surface of the gold electrode. This performance of the composite-modified electrode could be attributed to the synergistic interaction of the features of MOFs and TQDs, endowing the composite with characteristics such as a high surface area, tuneability, low toxicity, high conductivity and high photostability.[94]

3.10 Optimization of the analytical parameters

In order to maximise the sensitivity and efficiency, critical parameters such as pH, contact time, and sensor materials (composite) concentration at the surface of the modified gold electrode must be precisely calibrated when employing sensor-based techniques for bisphenol A (BPA) determination.

3.10.1 Effect of pH. An ideal pH will ensure maximum interactions between BPA molecules and the modified electrode sensor's active sites. The pH of the solution has a significant impact on the ionisation state of the BPA and the surface charge of the sensor, which influences binding affinity and electrochemical response.[95] In order to determine the preferred pH of the solution, PBS buffer solutions with a pH range from 2 to 12 and a gradient range of 1.0 were established for this study. According to the data displayed in Fig. 8(A), the oxidation peak current response value attained its maximum when the pH of the PBS buffer solution approached 8. Thus, pH 8 was selected as the ideal pH for this study. At pH values above 8, the amount of BPA at the surface of the composite-modified gold electrode decreases.

3.10.2 Effect of concentration of the composite at the surface of the modified electrode. The concentration of the composite at the surface of the modified electrode is important because higher concentrations can enhance the signal strength

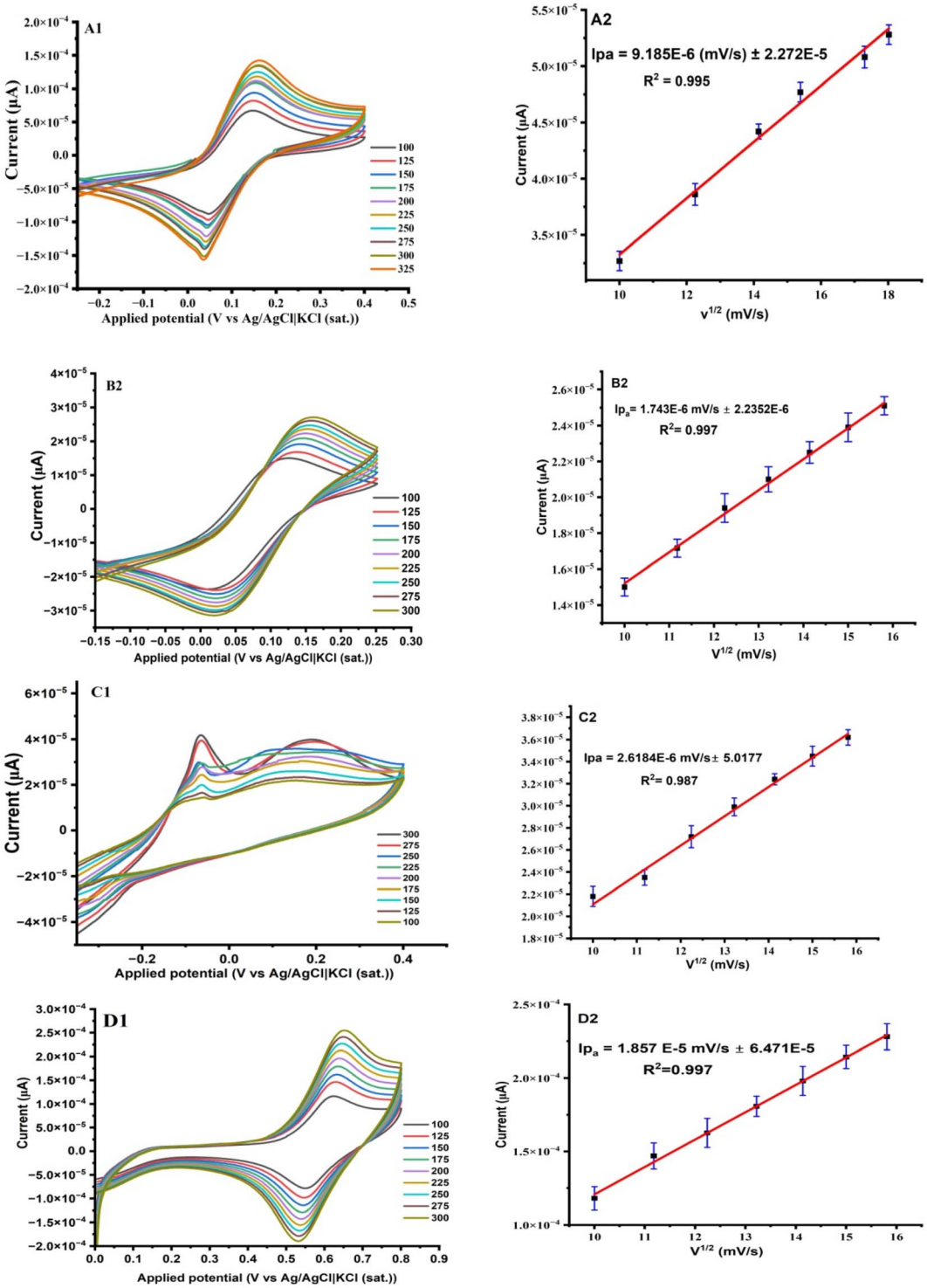

Fig. 6 Electrochemical responses of 5 mM potassium ferricyanide $K_3[Fe(CN)_6]$ in 0.1 M potassium chloride (KCl) at the surface of the bare electrode and electrodes modified with compounds **1**, **2**, and **3** (A1–D1). Plots of the oxidation peak currents *vs.* square root of scan rates (A2–D2) at pH 7, indicating the behaviour of the modified electrodes for BPA application.

up to a threshold point, beyond which aggregation or nonspecific binding emerges.[96] To conduct this experiment, 8 μL of various composite concentrations, from 2 to 10 mg L^{-1}, were prepared and dropped over the surface of the electrode. Fig. 8(B) shows that the oxidation peak current response increases with increasing concentration of the composite and reaches a maximum at a concentration of 6 mg L^{-1}. Further increases in concentration caused the oxidation peak current to decrease. The most suitable composite concentration for successful and efficient BPA detection is 6 mg L^{-1}.

Table 2 Cyclic voltammetry results of potassium ferricyanide at the surface of the electrodes modified with compounds **1**, **2**, and **3** at 200 mV s^{-1}, illustrating the performance and efficiency of each modified electrodes

	Oxidation response		Reduction response		Potential separation
Modified electrodes	I_{pa} (μA)	E_{pa} (V)	I_{pc} (μA)	E_{pc} (V)	ΔE_p (V) = $E_{pa} - E_{pc}$
MOFs/AuE	2.25×10^{-5}	0.148	-2.74×10^{-5}	0.0209	0.127
TQDs/AuE	3.301×10^{-5}	0.188	—	—	—
TQDs@MOFs/AuE	1.94×10^{-4}	0.64	1.428×10^{-4}	0.540	0.100

3.10.3 Effect of contact time of reaction. The duration of the analyte-sensor interactions is determined by the contact time of the reaction, which must strike a balance between operational efficiency and adequate binding for observable signals to avert unnecessary delays once equilibrium is achieved. Prolonged contact time may cause BPA particles to redeposit on the modified electrode surface, wasting time, whereas insufficient contact time can prevent the composite from adequately interacting with BPA particles in the solution, leading to a low detection rate.[97] Oxidation peak current response (I_{pa}) increases with an increase in the contact time of the reaction (0–220 s) and reaches a plateau at 120 s (Fig. 8(C)). With further contact time of reaction, the oxidation peak current decreases and stabilises. This could signify that the composite-modified electrode surface is saturated, which makes it more difficult to detect more BPA particles. Thus, the ideal contact time for effective detection of BPA was determined to be 120 s.

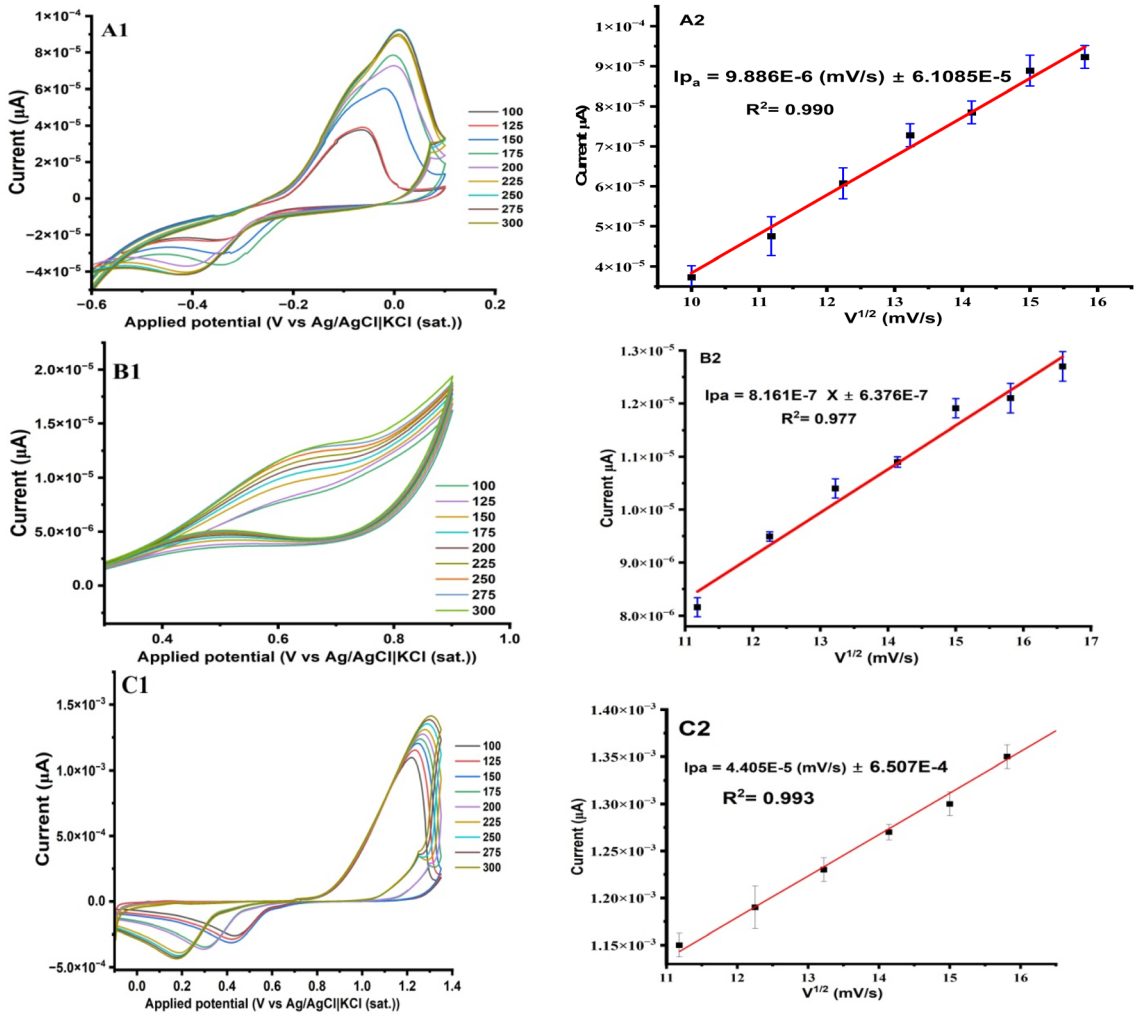

Fig. 7 Electrochemical response of 2 nM BPA in 0.1 M PBS at pH 7 at the electrodes modified with compounds **1**, **2**, and **3** (A1–C1). Plots of the oxidation peak currents *vs.* square root of scan rate (A2–C2), illustrating the greater performance and efficiency of the electrode modified with **3** than those of the electrodes modified with **1** and **2**.

Table 3 Electrochemical responses for BPA determination at a 200 mV s^{-1} scan rate at the surface of the electrodes modified with compounds **1**, **2**, and **3**, depicting the higher performance of the electrode modified with **3**

	Electrode modified with **1** (MOFs)	Electrode modified with **2** (TQDs)	Electrode modified with **3** (TQDs@MOFs)
I_{pa} (μA)	7.26×10^{-5}	1.137×10^{-5}	1.27×10^{-3}
I_{pc} (μA)	-3.67×10^{-5}	—	-3.65×10^{-4}
E_{pa} (V)	9.11×10^{-5}	0.664	1.270-
E_{pc} (V)	−0.415	—	0.293

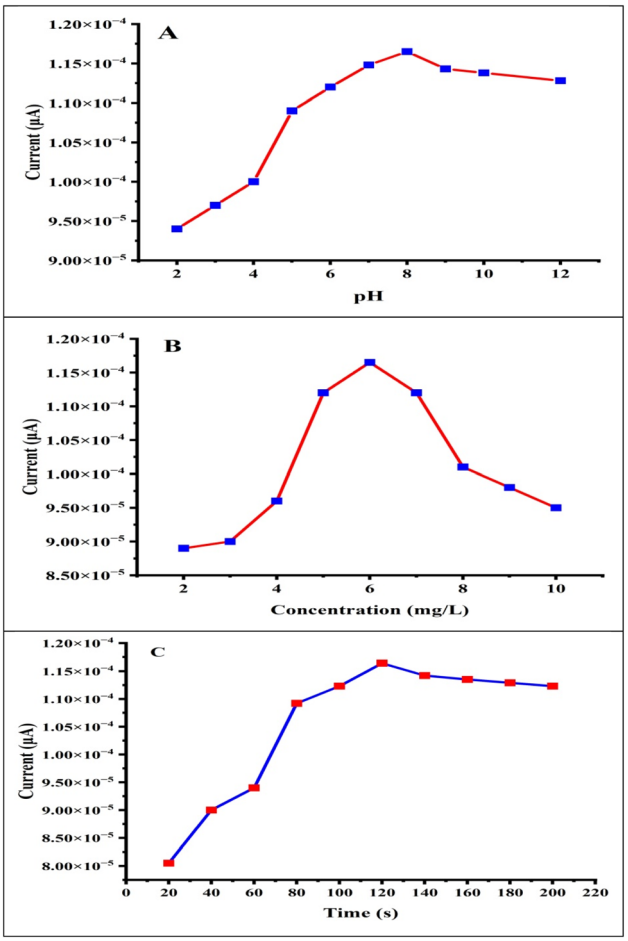

Fig. 8 PBS pH of 8 identified as the optimum pH for the excellent performance of the composite-modified electrode (A), 6 mg mL^{-1} of the composite at the surface of the electrode identified as the optimal concentration for excellent performance (B), and 120 s identified as the optimal contact time of reaction for the excellent performance of the composite-modified electrode (C) in the electrochemical determination of BPA.

3.10.4 Effect of concentration on the electrochemical determination of BPA and the calculated limit of detection using differential pulse voltammetry. The sensitivity and efficiency with which electrochemical techniques, in particular differential pulse voltammetry (DPV), can detect BPA have received some interest. The electrochemical response depends on BPA concentration, which also affects sensitivity, detection limits, and peak current response intensity.[98] In this study, we investigated the effects of BPA concentration on the electrochemical responses. Fig. 9(A) depicts the oxidation peak current response of different BPA concentrations in the range 2 to 20 nM. The linear regression plot showing the interaction between BPA concentrations and oxidation peak current response is shown in Fig. 9(B). The figure shows that an increase in the concentration of BPA leads to an increase in the electrochemical oxidation peak current response, which indicates a strong and excellent correlation between BPA concentrations and the electrochemical oxidation peak current response at the composite-modified electrode's surface.

The equation of the linear regression plot for the electrochemical oxidation peak current response is given as follows: $I_{pa} = 4.314 \times 10^{-7}$ nM ± 3.297×10^{-9} with the regression coefficient $R^2 = 0.995$. To determine the sensitivity of the electrochemical responses, we calculated the limit of detection (LOD)

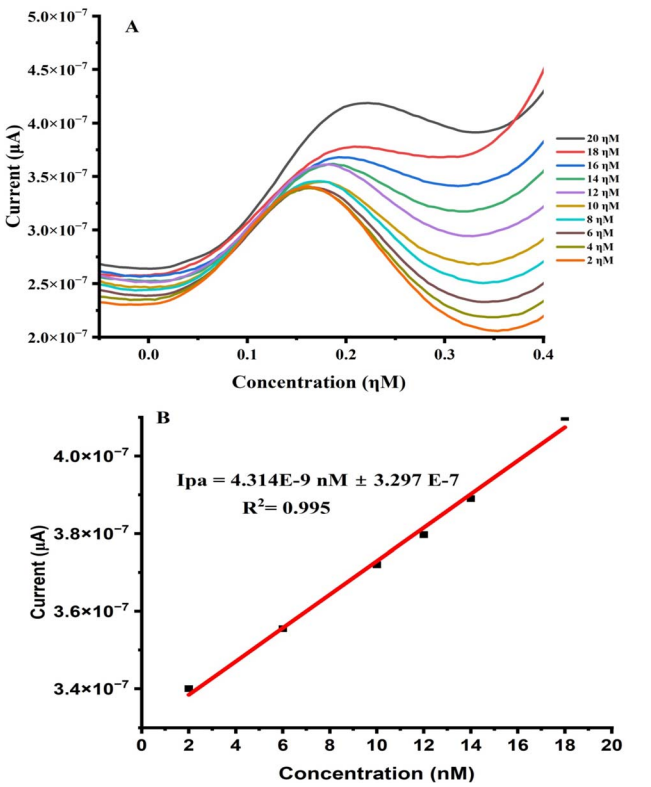

Fig. 9 Impact of concentration on the electrochemical determination of BPA (A), illustrating an increase in the response as the concentration increases, and the linear regression plot of the oxidation peak current response against concentration (B) using DPV.

and the limit of quantitation (LOQ) using eqn (1) and (2), respectively.[99,100]

$$\mathrm{LOD} = 3.3 \times (\mathrm{SD}/m) \quad (1)$$

$$\mathrm{LOQ} = 10 \times (\mathrm{SD}/m) \quad (2)$$

The LOD is the lowest concentration of an analyte that can be reliably detected from the background noise, and the LOQ is the lowest concentration of an analyte that can be quantitatively measured with acceptable precision and accuracy. SD is the standard deviation of the electrochemical oxidation peak current response, and m is the slope of the calibration curve. Using the equation, the calculated LOD and LOQ are 1.33 nM and 4.03 nM, respectively (S/N = 3). A comparison of the LOD and LOQ values obtained with this composite-modified electrode and those reported for other sensors in the literature is presented in Table 4. The results indicate that the LOD is significantly lower across a wide concentration range, suggesting that the electrochemical determination of BPA using this composite modified electrode is both sensitive and efficient.

3.10.5 Stability studies of the composite-modified gold electrode. The ability of an electrochemical sensor or electrode to operate consistently over time, even after extended storage or recurrent use, is referred to as stability in electrochemical determination.[109]

For this study, cyclic voltammetry was used to examine the stability of the composite-modified electrode using 5 mM $K_3[Fe(CN)_6]$ in 0.1 M KCl at pH 8. Over a potential window from −0.5 V to 0.1 V, 20 consecutive cyclic runs were carried out at 200 mV s^{-1}, and a redox response was obtained for each of the twenty successive runs with little variation in the oxidation peak current response between the last 20 runs (Fig. 10). The 5th and 20th cyclic voltammograms exhibited oxidation peak current responses of 5.84×10^{-6} μA and 6.04×10^{-6} μA, respectively, which confirmed the composite-modified electrode showed 95% stability, as evidenced by the estimated 3.31% variation in the oxidation peak current intensity over the course of the 15 consecutive runs. This confirms that the composite-modified electrode is stable and could be used for additional cyclic runs.

3.10.6 Reproducibility studies on the composite-modified electrode. An electrochemical sensor's reproducibility is reflected in the determination of an analyte over multiple trials, sensor batches, or experimental configurations.[110] To evaluate the reproducibility of the composite-modified electrode, DPV was employed to study the oxidation peak current responses of 5 mM $K_3[Fe(CN)_6]$ in 0.1 M KCl at pH 8 using five different electrodes over a potential range from −0.1 V to 0.4 V (Fig. S11A). The oxidation peak current responses of the five different electrodes used are 6.82×10^{-7} μA, 6.87×10^{-7} μA, 6.91×10^{-7} μA, 6.95×10^{-7} μA, and 6.96×10^{-7} μA for electrodes A, B, C, D, and E, respectively (Fig. S11B). The difference between the responses of electrode A and electrode E is 2%, which indicates that the modified electrode is 98% reproducible over the five different electrodes used.

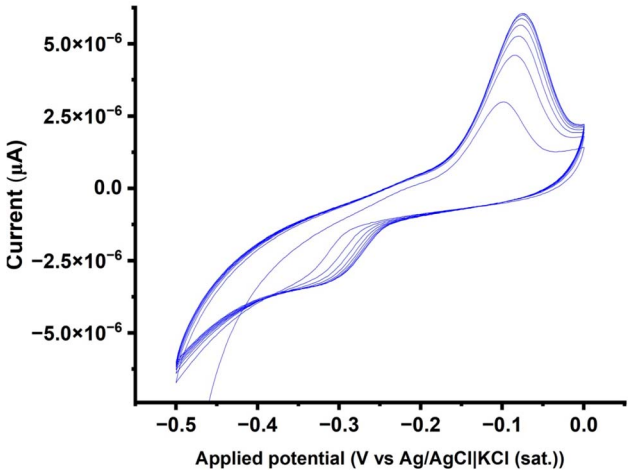

Fig. 10 Stability of the composite-modified electrode for 20 consecutive runs, depicting the good stability of the modified-electrode.

3.10.7 Selectivity studies of the composite-modified electrode. Selectivity is the ability of a modified electrode to selectively identify the target analyte in the presence of interfering chemicals while reducing the impact of other substances with comparable electrochemical characteristics.[111] The CV technique was employed for this study over a potential range from −0.4 V to 1.3 V at 200 mV s^{-1} using tetramethyl thiourea, urea, and 1,3-dimethyl-2-thiourea as interfering substances (analyte)

Table 4 Comparison of the LOD and LOQ values of the developed composite-modified electrode with those of the other reported sensors for the determination of BPA

Modified electrode	Linear range	Method used	Detection limit	Ref.
CNF/CPE	0.1–60 μM	DPV	50 nM	101
$Li_4Ti_5O_{12}$/MWCNTs/GCE	0.1–10 μM	DPV	78 nM	102
MIP-MWNPE	0.08–100 μM	DPV	22 nM	103
PGA/MWCNTNH$_2$/GC	0.1–10 μM	DPV	20 nM	104
SiO_2/rGO–AuNPs/GCE	0.03–10 μM 10–120 μM	DPV	5 nM	105
GR-IL/GCE	0.02–2 μM	LSV	8 nM	106
Ferrocenyl methyl methacrylate	4.7–8 nmol L^{-1}	C. V.	3.2 nmol L^{-1}	107
Rh_2O_3–rGO/GCE	0.6–40 μM	C. V	0.12 μM	108
[$AgInS_2$ @[Cu_4(NITA)$_4$(H_2O)$_2$(DMF)$_4$(DMF)$_4$]]	4–16 nM	DPV	1.33 nM	This work

Table 5 Determination of BPA in three different water samples ($n = 5$), with a percentage recovery between 97.52–99.88% and relative standard deviation varying from 1.93% to 4.65%

Water samples	Measured (μM)	Spiked (μM)	Found (μM)	%Recovery	RSD ($n = 5$)
Bottled water	0.00	0.00	0.000	—	—
		4.00	3.90	97.52	4.65%
		6.00	5.88	98.01	2.31%
Untreated wastewater	8.512	0.00	8.495	99.80	3.16%
		4.00	12.49	99.88	2.97%
		6.00	14.45	99.58	3.05%
Treated wastewater	1.025	0.00	1.018	99.31	2.24%
		4.00	5.00	99.52	1.93%
		6.00	6.997	99.60	2.91%

in the presence of bisphenol A (BPA) (Fig. S12). In electrochemistry, thiourea could often play the role of an electrode modifier, in which they create new active sites at the surface of the electrode (activation effect) to enhance the sensitivity and selectivity towards the analyte (BPA), and hence, it is usually referred to as a brightener or accelerator.[112] BPA samples with a concentration of 1 μM and samples of other interfering substances at a concentration of 5 μM were prepared. From the results (Fig. S12), it could be observed that the composite-modified electrode has the highest oxidation peak current response for BPA (1.56×10^{-5} μA), while its oxidation peak current responses for the other interfering substances were negligible compared to that of the preferred analyte (see inset in Fig. S12). This outstanding response for bisphenol A could be due to the strong interaction between the molecules of BPA and the composite at the surface of the modified electrode, related to the electronic features and conductivity of the molecules.[113]

3.10.8 Water sample BPA assessment. In order to establish the reliability and usefulness of the synthesized composite-modified electrode as a sensor, water samples that are representative of everyday life were tested. The analysis was conducted using bottled water, untreated wastewater, and treated wastewater from the uMngeni-uThukela water treatment plant in Pietermaritzburg, South Africa. Prior to the analysis, the water samples were filtered using a 0.22 μm filtering membrane to exclude any contaminants. The analysis was conducted using a well-known standard addition method (SAM). Known concentrations of BPA ranging from 4 μM to 6 μM were added to 5 mL of phosphate buffer solution (PBS) (pH 8) along with a volume of 5 mL of each water sample. The results were recorded using DPV (Table 5). Before the spiked concentrations were added, BPA was detected in trace amounts in the untreated and treated wastewater samples. The practical capability of the modified electrode sensor was determined by measuring the responses in all samples at the surface of the composite-modified electrodes upon the addition of different concentrations of BPA. The relative standard deviation percentage (% RSD) for five parallel detections ($n = 5$) was between 1.93% and 4.65%, which is below 5.00%, and the recovery percentage was in the range 97.52–99.88%, which indicates that the recovery response is excellent.[114] Thus, the use of this composite-modified electrode could result in significant and noteworthy BPA sensing responses in actual water samples.

4 Conclusion

A copper(II) metal–organic framework (MOF) in which the copper(II) ion is bidentately bonded to 5-nitroisophthalic acid was synthesized and characterized by single-crystal X-ray crystallography. The molecular structure of the compound revealed a dimeric copper(II) complex, $[Cu_4(NITA)_4(H_2O)_2(DMF)_4]\cdot(DMF)_4$, in which four copper(II) ions are coordinated to four molecules of 5-nitroisophthalic acid, two water molecules, and four molecules of dimethylformamide. The copper(II) metal organic framework crystallized with four molecules of dimethylformamide as a solvent of crystallization. The copper(II) metal–organic framework (MOF), ternary quantum dot (TQD) of silver indium sulphide, and their composite (TQDs@MOF) were synthesized, characterized, and used as modified gold electrodes. The modified gold electrode was used as an electrochemical sensor for the determination of bisphenol A (BPA). The study revealed that the composite-modified gold electrode exhibits excellent performance for the determination of BPA, in contrast to the MOFs and TQDs. This could be ascribed to the synergistic interactions of the properties of the ternary quantum dot and the metal–organic framework in the composite. A diffusion-controlled process is observed at the surface of the composite-modified electrode in the presence of bisphenol A, based on its electrochemical characteristics and responses. The limit of detection (LOD) and limit of quantitation (LOQ) are 1.33 nM and 4.03 nM, respectively, over a concentration range of 2 nM to 20 nM (S/N = 3). These results confirm that the detection using the composite-modified electrode offers modest results, and it has the potential to be further developed as an efficient sensor for BPA detection in water. The electrochemical detection procedure is reproducible, and the composite-modified electrode is stable and selective towards BPA determination.

Conflicts of interest

We declare no conflicts of interest.

Data availability

CCDC 2307117 contains the supplementary crystallographic data for this paper.[115]

All other data for the findings presented in this study are within the supplementary information (SI). Supplementary information: packing diagram showing the number of $[Cu_4(NITA)_4(H_2O)_2(DMF)_4]\cdot(DMF)_4$ (**1**) in a unit cell (Fig. S1). Polyhedral representation of $[\{Cu_4(NITA)_4(H_2O)_2\}(DMF)_4]\cdot(DMF)_4$] illustrating the distortion of the square pyramidal (Fig. S2). A view of extended network of $[Cu_4(NITA)_4(H_2O)_2(DMF)_4]\cdot(DMF)_4$ along *a*-axis (Fig. S3). FTIR of $[Cu_4(NITA)_4(H_2O)_2(DMF)_4]\cdot(DMF)_4$] (MOFs) and NITA (ligand), illustration the absorbances of various functional groups and evidence of coordination (Fig. S4). FTIR of Ternary quantum dots ($AgInS_2$), glutathione and gelatine depicting the absorbances various functional groups (Fig. S5). FTIR of MOFs $[Cu_4(NITA)_4(H_2O)_2(DMF)_4]\cdot(DMF)_4$, TQDs ($AgInS_2$), and TQDs@MOFs $\{AgInS_2[Cu_4(NITA)_4(H_2O)_2(DMF)_4]\cdot(DMF)_4\}$, depicting the interaction between the MOFs and TQDs in the newly synthesized TQDs@MOFs (Fig. S6). UV-Vis of MOFs $[Cu_4(NITA)_4(H_2O)_2(DMF)_4]\cdot(DMF)_4$ (A), TQDs ($AgInS_2$) (B), and TQDs@MOFs $\{AgInS_2[Cu_4(NITA)_4(H_2O)_2(DMF)_4]\cdot(DMF)_4\}$ (C), illustrating the different electronic transitions in MOFs, TQDs which were also experience in the spectrum of TQDs@MOFs (Fig. S7). Band gaps of MOFs $[Cu_4(NITA)_4(H_2O)_2(DMF)_4]\cdot(DMF)_4$, TQDs ($AgInS_2$), and TQDs@MOFs $\{AgInS_2[Cu_4(NITA)_4(H_2O)_2(DMF)_4]\cdot(DMF)_4\}$ depicting the interaction between MOFs and TQDs (Fig. S8). PXRD of MOFs $[Cu_4(NITA)_4(H_2O)_2(DMF)_4]\cdot(DMF)_4$, TQDs ($AgInS_2$), and TQDs@MOFs $\{AgInS_2[Cu_4(NITA)_4(H_2O)_2(DMF)_4]\cdot(DMF)_4\}$, illustrating the presence of the phases of MOFs and TQDs in the diffraction pattern of TQDs@MOFs indicating the interacting of the MOFs and TQDs (Fig. S9). SEM and TEM images depicting the morphology, surface texture, and arrangement of compounds 1(A1,A2), 2(B1, B2), 3(C1, C2) (Fig. S10). Reproducibility of the composite compounds at the surface of 5 different electrodes with little variation in response (Fig. S11). Selectivity of composite modified electrode for BPA with high response in the presence of three interfering substances (Fig. S12). Crystal data and structure refinement of $[Cu_4(NITA)_4(H_2O)_2(DMF)_4]\cdot(DMF)_4$ illustration details of the single crystal (Table T1). Some selected bond lengths and bond angles explaining the geometry of $[Cu_4(NITA)_4(H_2O)_2(DMF)_4]\cdot(DMF)_4$ (Table T2). See DOI: https://doi.org/10.1039/d5ra05819h.

Acknowledgements

This study was financially supported by the National Research Foundation, South Africa, through the competitive support for rated researcher, grant number CPRR23042396404.

References

1 W. Bunmahotama, T. -F. Lin and X. Yang, *Chemosphere*, 2020, **238**, 124658.
2 J. Zhang, H. Wu, L. Shi, Z. Wu, S. Zhang, S. Wang and H. Sun, *Sep. Purif. Technol.*, 2024, **329**, 125225.
3 F. Zhao, S. Fang, Y. Gao and J. Bi, *J. Colloid Interface Sci.*, 2022, **615**, 876–886.
4 C. Xiao, L. Wang, Q. Zhou and X. Huang, *J. Hazard. Mater.*, 2020, **384**, 121488.
5 N. Kataria, D. Bhushan, R. Gupta, S. Rajendran, M. Y. M. Teo and K. S. Khoo, *Environ. Pollut.*, 2022, **315**, 120319.
6 N. B. Messaoud, M. E. Ghica, C. Dridi, M. B. Ali and C. M. A. Brett, *Sens. Actuators, B*, 2017, **253**, 513–522.
7 D. D. Seachrist, K. W. Bonk, S.-M. Ho, G. S. Prins, A. M. Soto and R. A. Keri, *Reprod. Toxicol.*, 2016, **59**, 167–182.
8 C. J. Catenza, A. Farooq, N. S. Shubear and K. K. Donkor, *Chemosphere*, 2021, **268**, 129273.
9 C. S. Rosenfeld, *Front. Neurosci.*, 2015, **9**, 1–15.
10 L. F. Loffredo, M. E. Coden and S. Berdnikovs, *Nutrients*, 2020, **12**(2), 343.
11 C. Lambré, J. M. B. Baviera, C. Bolognesi, A. Chesson, P. S. Cocconcelli, R. Crebelli, D. M. Gott, K. Grob, E. Lampi, M. Mengelers, A. Mortensen, G. Rivière, V. Silano, I. Steffensen, C. Tlustos, L. Vernis, H. Zorn, M. Batke, M. Bignami, E. Corsini, R. FitzGerald, U. Gundert-Remy, T. Halldorsson, A. Hart, E. Ntzani, E. Scanziani, H. Schroeder, B. Ulbrich, D. Waalkens-Berendsen, D. Woelfie, Z. Al Harraq, K. Baert, M. Carfi, A. F. Castoldi, C. Croera and H. V. Loveren, *EFSA J.*, 2023, 6857.
12 M. C. Estevez, R. Galve, F. Sanchez-Baeza and M. P. Marco, *Anal. Chem.*, 2005, **77**, 5283–5293.
13 C. Lu, J. G. Li, Y. Yang and J. M. Lin, *Talanta*, 2010, **82**, 1576–1580.
14 K. Inoue, K. Kato, Y. Yoshimura, T. Makino and H. Nakazawa, *J. Chromatogr. B*, 2000, **749**, 17–23.
15 W. H. Zhao, N. Sheng and R. Zhu, *J. Hazard. Mater.*, 2010, **179**, 223–229.
16 M. Liu, Y. Hashi and F. Y. Pan, *J. Chromatogr. A*, 2006, **1133**, 142–148.
17 R. J. W. Meesters and H. F. Schroder, *Anal. Chem.*, 2002, **74**, 3566–3574.
18 S. C. Cunha and J. O. Fernandes, *Talanta*, 2010, **83**, 117–125.
19 S. H. Wang, X. T. Wei, L. Y. Du and H. Zhuang, *Luminescence*, 2005, **20**, 46–50.
20 N. Tsuru, M. Kikuchi, H. Kawaguchi and S. Shiratori, *Thin Solid Films*, 2006, **499**, 380–385.
21 M. A. Rahman, M. J. A. Shiddiky, J. S. Park and Y. B. Shim, *Biosens. Bioelectron.*, 2007, **22**, 2464–2470.
22 B. K. Kang, J. H. Kim, S. Kim and K. H. Yoo, *Appl. Phys. Lett.*, 2011, **98**, 073703.
23 X. Wang, H. L. Zeng, L. X. Zhao and J. M. Lin, *Anal. Chim. Acta*, 2006, **556**, 313–318.
24 H. X. Fan, Y. Li, D. Wu, H. M. Ma, K. X. Mao, D. W. Fan, B. Du, H. Li and Q. Wei, *Anal. Chim. Acta*, 2012, **711**, 24–28.
25 Q. X. Wang, Y. H. Wang, S. Y. Liu, L. H. Wang, F. Gao, F. Gao and W. Sun, *Thin Solid Films*, 2012, **520**, 4459–4464.
26 C. X. Huang, Y. T. Wu, J. S. Chen, Z. Z. Han, J. Wang, H. B. Pan and M. Du, *Electroanalysis*, 2012, **24**, 1416–1423.
27 J. Heine and K. Mueller-Buschbaum, *Chem. Soc. Rev.*, 2013, **42**, 9232–9242.

28 Z. W. Wei, C. X. Chen, S. P. Zheng, H. P. Wang, Y. N. Fan, Y. Y. Ai, M. Pan and C. Y. Su, *Inorg. Chem.*, 2016, **55**, 7311–7313.
29 K. Liu, X. J. Zhang, X. X. Meng, W. Shi, P. Cheng and A. K. Powell, *Chem. Soc. Rev.*, 2016, **45**, 2423–2439.
30 J. W. Liu, L. F. Chen, H. Cui, J. Y. Zahng, L. Zahng and C. Y. Su, *Chem. Soc. Rev.*, 2014, **43**, 6011–6061.
31 Z. Y. Zhang, H. Yoshikama and K. Awaga, *J. Am. Chem. Soc.*, 2014, **136**, 16112–16115.
32 D. Cunha, M. B. Yahia, S. Hall, S. Hall, S. R. Miller, H. Chevreau, E. Elkaïm, G. Maurin, P. Horcajada and C. Serre, *Chem. Mater.*, 2013, **25**, 2767–2776.
33 J. W. Wu, H. B. Zhang and S. W. Du, *J. Mater. Chem. C*, 2016, **4**, 3364–3374.
34 X. Y. Ren and L. H. Lu, *Chin. Chem. Lett.*, 2015, **26**, 1439–1445.
35 Z. Lu, K. Wang, Y. Cao, Y. Li and D. Jia, *J. Alloys Compd.*, 2021, **871**, 159580.
36 K. S. Asha, R. Bhattacharjee and S. Mandal, *Angew. Chem., Int. Ed.*, 2016, **55**, 11528–11532.
37 J. M. Zhou, H. H. Li, H. Zhang, H. M. Li, W. Shi and P. Cheng, *Adv. Mater.*, 2015, **27**, 7072–7077.
38 H. Y. Li, Y. L. Wei, X. Y. Dong, S. Q. Zang and T. C. W. Mak, *Chem. Mater.*, 2015, **27**, 1327–1331.
39 T. Rasheed and F. Nabeel, *Coord. Chem. Rev.*, 2019, **401**, 213065.
40 Q. Wang, Q. Y. Gao, A. M. Al-Enizi, A. Nafady and S. Q. Ma, *Inorg. Chem. Front.*, 2020, **7**, 300–339.
41 Y.-H. Zhai, Y.-X. Peng, Y. Hong, Y.-M. Chen, G.-Y. Zhou, W. He, P.-J. Wang, X.-M. Chen and C. Wang, *J. Electrochem.*, 2023, **29**(8), 2208111.
42 D. M. Schubert, M. Z. Visi and C. B. Knobler, *Main Group Chem.*, 2008, **7**(4), 311–322.
43 X. Song, M. Oh and M. S. Lah, *Inorg. Chem.*, 2013, **52**(19), 10869–10876.
44 G. Lee, C. V. Varanasi and J. Liu, *Nanoscale*, 2015, **7**(7), 3181–3188.
45 V. G. Reshma and P. V. Mohanan, *J. Lumin.*, 2019, **205**, 287–298.
46 E. Petryayeva, W. R. Algar and I. L. Medintz, *Appl. Spectrosc.*, 2013, **67**, 215–252.
47 Z. Wang, X. Sun, Y. Xu, L. Yang, M. Wang, Y. Xia, Y. Wang, Y. Tang, C. Qiao and Y. Lin, *Colloids Surf., A*, 2024, **696**, 134292.
48 Y. Ma, Y. Leng, D. Huo, D. Zhao, J. Zheng, P. Zhao, H. Yang, F. Li and C. Hou, *Food Chem.*, 2023, **429**, 136850.
49 C. Frigerio, D. S. Ribeiro, S. S. M. Rodrigues, V. L. Abreu, J. A. Barbosa, J. A. Prior and J. L. Santos, *Anal. Chim. Acta*, 2012, **735**, 9–22.
50 J. Donegan and Y. Rakovich, *Cadmium Telluride Quantum Dots: Advances and Applications*, CRC Press, Boca Raton, FL, USA, 2013, pp. 206–229.
51 S. Mondal, S. Naska, A. K. Dey, E. Sinn, C. Eribal, S. R. Herron and S. K. Chattopadhyay, *Inorg. Chim. Acta*, 2013, **398**, 98–105.
52 SAINT, Bruker AXS Inc., Madison, WI, USA, v 2019,1-0.
53 G. M. Sheldrick, SHELXS-97, SHELXL-2014 and SADABS, *Acta Crystallogr.*, 2014, **C71**, 3–8.
54 L. J. Barbour, *J. Supramol. Chem.*, 2001, **1**, 189–191.
55 J. L. Atwood and L. J. Barbour, *Cryst. Growth Des.*, 2003, **3**(1), 3–8.
56 Persistence of Vision Pty. Ltd, Persistence of Vision Raytracer, Version 3.6, retrieved from **http://www.povray.org/download**, 2014.
57 R. C. Castro, R. N. M. J. Páscoa, M. L. M. F. S. Saraiva, J. L. M. Santos and D. S. M. Ribeiro, *Spectrochim. Acta, Part A*, 2022, **267**, 120592.
58 X. Fu, H. Li, R. Lv, D. Hong, B. Yang, W. Gu and X. Liu, *J. Solid State Chem.*, 2018, **264**, 35–41.
59 Z. Staszak, A. Krojcer, M. Kubiak, A. Puszko, G. Maciejewska and M. Cieslak-Golonka, *Struct. Chem.*, 2010, **21**, 305–313.
60 J. Wang, F. Su and L. Shi, *Acta Crystallogr.*, 2018, **74**, 691–694.
61 J.-l. Wang, C. R. Wang, Z. J. Wanga and B. S. Yang, *Acta Crystallogr.*, 2013, **69**, m19.
62 W. Lu, J. Tang, Z. Gu, L. Sun, H. Wei, Y. Wang, S. Yang, X. Chi and L. Xu, *J. Inorg. Biochem.*, 2023, **238**, 112030.
63 A. K. Seguin, K. W. Araneda, D. C. Arriagada, C. Cruz, D. V. Yazigi and V. P. A García, *J. Mol. Struct.*, 2021, **1224**(15), 129172.
64 Ö. F. E. Özbek, *J. Chem. Sci.*, 2020, **132**, 61.
65 S. Zhu, H. Hu, J. Hu, J. Li, F. Hu and Y. Wang, *J. Coord. Chem.*, 2017, **70**(19), 3325–3337.
66 L. J. Ma, X. Li, Y. J. Yan, Y. N. Yue and W. K. Dong, *J. Mol. Struct.*, 2023, **1275**(5), 134617.
67 Y. Yang, C. Tu, Z. Liu, J. Wang, X. Yang and F. Cheng, *Polyhedron*, 2021, **206**, 115339.
68 C. P. Delaney, E. Lin, Q. Huang, I. F. Yu, G. Rao, L. Tao, A. Jed, S. M. Fantasia, K. A. Püntener and J. F. Hartwig, *Science*, 2023, **381**, 1079–1085.
69 G. Chakraborty, I.-H. Park, R. Medishetty and J. J. Vitta, *Chem. Rev.*, 2021, **121**(7), 3751–3891.
70 K. Nakamoto, *Infrared and Raman Spectra of Inorganic and Coordination Compounds*, Wiley, New York, 5th edn, 1997.
71 W. W. Xiong, G. H. Yang, X. C. Wu and J. J. Zhu, *ACS Appl. Mater. Interfaces*, 2013, **5**, 8210–8216.
72 O. Yarema, M. Yarema and V. Wood, *Materials*, 2018, **30**, 1446–1461.
73 L. Jia, Y. Wang, Q. Nie, B. Liu, E. Liu, X. Hu and J. Fan, *Mater. Lett.*, 2017, **200**, 27–30.
74 S. Liu, H. Zhang, Y. Qiao and X. Su, *RSC Adv.*, 2012, **2**, 819–825.
75 T. Jiang, J. Song, H. Wang, X. Ye, H. Wang, W. Zhang, M. Yang, R. Xia, L. Zhu and X. Xu, *J. Mater. Chem. B*, 2015, **3**, 2402–2410.
76 J. Wen, D. Jiang, X. Shan, W. Wang, F. Xu, H. hiigi and Z. Chen, *Microchem. J.*, 2022, **172**, 106927.
77 M. D. Olawale, A. C. Tella, J. A. Obaleye and J. S. Olatunji, *New J. Chem.*, 2020, **44**, 3961.
78 A. C. Tella, S. O. Owalude, A. C. Ojekanmi and O. S. Oluwafemi, *New J. Chem.*, 2014, **38**, 4494–4500.
79 K. Nose, T. Omata and S. O.-Y. Matsuo, *J. Phys. Chem. C*, 2009, **113**(9), 3455–3460.

80 Z. Wu, L. M. Xu, J. D. Wang and J. Song, *Opto-Electron. Adv.*, 2024, **7**, 240050.
81 Y. Ma, G. Xu, F. Wei, Y. Cen, Y. Ma, Y. Song, X. Xu, M. Shi, S. Muhammad and Q. Hu, *J. Mater. Chem. C*, 2017, **5**, 8566.
82 N. Vogel, M. Retsch, C.-A. Fustin, A. del Campo and U. Jonas, *Chem. Rev.*, 2015, **115**(13), 6265–6311.
83 Z. Li, Q. Fan and Y. Yin, *Chem. Rev.*, 2022, **122**(5), 4976–5067.
84 N. B. Alsharif, S. Muráth, B. Katana and I. Szilagyi, *Adv. Colloid Interface Sci.*, 2021, **294**, 102456.
85 C.-J. Chang, J.-K. Chen, K.-S. Lin, Y.-H. Wei, P.-Y. Chao and C.-Y. Huang, *J. Alloys Compd.*, 2020, **813**, 152186.
86 L. Gianelli, V. Amendola, L. Fabbrizzi, P. Pallavicini and G. G. Mellerio, *Rapid Commun. Mass Spectrom.*, 2001, **15**, 2347–2353.
87 P. S. Adarakatti, *Agricul. Electrochm.*, ACS Symposium Series, 2025, vol. 1496, ch. 2, pp. 17–46.
88 W. Wang, J. Cao, J. Yu, F. Tian, X. Luo, Y. Hao, J. Huang, F. Wang, W. Zhou and J. Xu, *Polymers*, 2023, **15**, 1856.
89 N. O. Laschuk, E. B. Easton and O. V. Zenkina, *RSC Adv.*, 2021, **11**, 27925–27936.
90 N. Dutta, R. R. Suresh and G. Dutta, *J. Electroanal. Chem.*, 2024, **969**, 18540.
91 D. J. Joshi, J. R. Koduru, N. I. Malek, C. M. Hussain and S. K. Kailasa, *TrAC, Trends Anal. Chem.*, 2021, **144**, 116412.
92 R. Jarošová, K. Bhardwaj and G. M. Swain, *J. Electroanal. Chem.*, 2020, **875**, 114744.
93 A. V. Kosov, O. V. Grishenkova, O. L. Semerikova, V. A. Isaev and Y. P. Zaikov, *J. Electroanal. Chem.*, 2021, **883**, 115056.
94 M. Shirani, A. Aslani, S. Sepahi, E. Parandi, A. Motamedi, E. Jahanmard, H. R. Nodeh and B. Akbari-Adergani, *Anal. Methods*, 2022, **14**, 2623–2630.
95 N. Ambauen, J. Muff, F. Tscheikner-Gratl, T. T. Trinh, C. Hallé and T. Meyn, *J. Environ. Chem. Eng.*, 2020, **8**(5), 104183.
96 Md. Y. Ali, A. U. Alam and M. M. R. Howlader, *Sens. Actuators, B*, 2020, **320**(1), 128319.
97 D. Verma, A. K. Yadav, M. D. Mukherjee and P. R. Solanki, *J. Environ. Chem. Eng.*, 2021, **9**(4), 105504.
98 O. Moradi, *Food Chem. Toxicol.*, 2022, **165**, 113074.
99 R. H. Ye, I. Y. Chen, D. H. Huang, Y. J. Wang and S. Chen, *Biosensors*, 2022, **12**, 367.
100 S. Tajik, H. Beitollahi, F. G. Nejad, K. Zhang, Q. V. Le, H. W. Jang, S. Y. Kim and M. Shokouhimehr, *Sensors*, 2020, **20**, 3364.
101 J. Sun, Y. Liu, S. Lv, Z. Huang, L. Cui and T. Wu, *Electroanalysis*, 2016, **28**(3), 439–444.
102 W. Wang, X. Yang, Y. Gu, C. Ding and J. Wan, *Ionics*, 2015, **21**, 885–893.
103 Z. C. Chen, Y. Tang, H. Zeng, Z. Liu, L. Yin and N. Li, *Anal. Lett.*, 2014, **47**(6), 996–1014.
104 Y. Lin, K. Liu, C. Liu, L. Yin, Q. Kang, L. Li and B. Li, *Electrochim. Acta*, 2014, **133**, 492–500.
105 E. Liu and X. Zhang, *Anal. Methods*, 2014, **6**, 8604–8612.
106 P. Jing, X. Zhang, Z. Wu, L. Bao, Y. Xu, C. Liang and W. Cao, *Talanta*, 2015, **141**, 41–46.
107 L. J. Ling, J. P. Xu, Y. H. Deng, Q. Peng, J. H. Chen, S. Y. He and Y. J. Nie, *Anal. Methods*, 2018, **10**, 2722–2730.
108 R. Shi, X. Yuan, A. Liu, M. Xu and Z. Zhao, *Appl. Sci.*, 2018, **8**, 2535.
109 H. Ezoji, M. Rahimnejad and G. Najafpour-Darzi, *Ecotoxicol. Environ. Saf.*, 2020, **190**, 110088.
110 S. He, H. Xia and F. Chang, *Microchem. J.*, 2022, **182**, 107858.
111 A. Eftekhari, M. Dalili, Z. Karimi, S. Rouhani, A. asanzadeh, S. Rostamnia, S. Khaksar, A. O. Idris, H. Karimi-Maleh, M. L. Yola and T. A. M. Msagati, *Food Chem.*, 2021, **358**, 129763.
112 Y.-H. Zhai, Y.-X. Peng, Y. Hong, Y.-M. Chen, G.-Y. Zhou, W. He, P.-J. Wang, X.-M. Chen and C. Wong, *J. Electrochem.*, 2023, **29**(8), 2208111.
113 A. Wang, Y. Wei and C. Wang, *J. Anal. Chem.*, 2015, **70**, 67–71.
114 S. Mabrouk, H. Rinnert, L. Balan, J. Jasniewski, G. Medjahdi and R. B. Chaabane, *J. Photochem. Photobiol., A*, 2022, **431**, 114050.
115 CCDC 2307117: Experimental Crystal Structure, 2025, DOI: **10.5517/ccdc.csd.cc2hfr4v**.